minerals

MDPI

Article

Genetic Association between Granites and Mineralization at the Gindi Akwati Cassiterite–Sulfide Deposit, North-Central Nigeria: Insights from Mineralogy, Fluid Inclusions, and Sulfur Isotopes

Abdulgafar Kayode Amuda [1,2], Shuang Li [3,*], Xiaoyong Yang [1,4,*], Jingya Cao [1,4] and Mohamed Faisal [5]

1 CAS Key Laboratory of Crust-Mantle Materials and Environments, School of Earth and Space Sciences, University of Science and Technology of China, Hefei 230026, China; amudaak@mail.ustc.edu.cn (A.K.A.); jingyacao@126.com (J.C.)
2 Department of Geology, Faculty of Earth and Environmental Sciences, Bayero University Kano, Kano 700241, Nigeria
3 Guangxi Key Laboratory of Hidden Metallic Ore Deposits Exploration, College of Earth Sciences, Guilin University of Technology, Guilin 541004, China
4 CAS Center for Excellence in Comparative Planetology, University of Science and Technology of China, Hefei 230026, China
5 Department of Geology, Faculty of Science, Suez Canal University, El-Ismailia 41522, Egypt; mohamed_faisal_89@science.suez.edu.eg
* Correspondence: lishuang@glut.edu.cn (S.L.); xyyang@ustc.edu.cn (X.Y.); Tel.: +86-0551-6465-2201 (X.Y.)

Citation: Amuda, A.K.; Li, S.; Yang, X.; Cao, J.; Faisal, M. Genetic Association between Granites and Mineralization at the Gindi Akwati Cassiterite–Sulfide Deposit, North-Central Nigeria: Insights from Mineralogy, Fluid Inclusions, and Sulfur Isotopes. *Minerals* **2022**, *12*, 761. https://doi.org/10.3390/min12060761

Academic Editors: Clemente Recio

Received: 19 April 2022
Accepted: 14 June 2022
Published: 15 June 2022

Abstract: The cassiterite–sulfide mineralization occurs within quartz veins and greisenized Precambrian Older Granite around the Gindi Akwati region at the Ropp complex's western boundary, north-central Nigeria. The intrusion of Jurassic Younger granite porphyry sheared the marginal parts of the Older Granite and the mylonitized zone created pathways for fluids that escaped during the late-stage consolidation of Jurassic biotite granite. The biotite granites are highly differentiated (K/Rb < 200), peraluminous (A/CNK > 1), high-K, and have high Sn concentrations (average = 117 ppm). The intrusion of Jurassic granite porphyry forced Older Granite interaction with ore-bearing fluid that escaped from Jurassic biotite granite under low oxygen fugacity at or below the NNO buffer. The above fluid–rock interaction caused mass changes in host granite during greisenization and redistributed ores in the vicinity of the shears. This suggests that chloride ions take the form of significant complex-forming ligands and efficiently sequestrate, transport, and deposit ore metals (Sn, Zn, Fe, and Cu) locally within the greisenized granites and quartz veins. The redox potential of the ores probably gave a false impression of metal zoning with a relatively higher abundance of the oxide ore than the sulfides at the surface. The alteration mineralogy (quartz-, topaz-, lepidolite-, and fluorite-bearing assemblages) coupled with S isotope and fluid inclusion systematic data suggests the hydrothermal history of "greisens" and veins started with hot (homogenization temperature ≥300 °C), low to moderate salinity (average = 4.08 wt. % NaCl), low density (≤0.6 g/cm^3) fluids and ≥ 200 bar trapping pressure. The sulfide isotopic composition ($\delta^{34}S_{V\text{-}CDT}$ = −1.30 to + 0.87 ‰) is very similar to typical magmatic fluids, indicating late-magmatic to early post-magmatic models of mineralization related to the anorogenic granite intrusions.

Keywords: cassiterite–sulfide mineralization; fluid inclusion; sulfur isotope; granite; north-central Nigeria

1. Introduction

Globally, granites, including their volcanic subvolcanic equivalents, account for over 99% of tin mine production either directly (primary ore) or indirectly (placer) [1]. Greisenization metasomatic processes are one of the most common wall rock alteration types, with a focus on tin-tungsten ore deposits [2]. The movement of hydrothermal solutions breaks the original granitic constituents to form new mineral assemblage and deposit various metals (Nb, Mn, Sn, Ta, W, Zn, and Cu with Fe) in the greisen [2–4]. The growing industrial demand for these metals, particularly REE, Nb, and Sn for sustainable development, necessitates a thorough examination of tectonic control and mineralization potential in granitic plutons [5].

The tin province of Nigeria is a classic example of recurrent tin mineralization, with two distinct episodes: Proterozoic-Cambrian Older Granite and pegmatites and Jurassic Younger Granites [6]. Other tin-mineralized provinces worldwide, such as South China, the Central Andes (Bolivia), and Malaysia, have experienced several tin mineralization episodes. These were attributed to the remobilization of previously existing regional tin anomalies [1,6]. A metallogenic synthesis in the plate-tectonic framework is still required to determine the geotectonic situation of these tin mineralized systems [1].

The primary sources of tin mineralization in and around the ring complexes in Nigeria are linked with Mesozoic anorogenic magmatic activity [4]. The youngest of these granites are biotite granites, which contain cassiterite and columbite-(Fe) as accessory phases in greisen and metasomatic zones, along with wolframite and sulfides [4]. The ores are mainly contained in lode-bearing veins and greisenized granites that filled the spaces between the cooling joints and fractures [4]. The reserves of cassiterite deposits in pegmatite and granites are given as 140,000 tons [7].

This contribution focuses on the genetic association between granites and mineralization at the Gindi Akwati cassiterite–sulfide deposit, north-central Nigeria. We investigate the petrogenesis and tectonic setting of the granites in this region. We also constrain the mechanism responsible for cassiterite–sulfide mineralization in the marginal greisenized Older Granite. We describe the nature and source of ore-forming fluids and the processes that cause cassiterite and sulfides to concentrate and precipitate in quartz veins and greisenized granites.

2. Geological Background

2.1. Regional Geology

The Ropp complex is one of the over fifty anorogenic ring complexes situated within the southern region of the Jos Plateau in Nigeria, Africa (Figure 1a,b). Mesozoic A-type peralkaline and alkaline granitic ring complexes were emplaced into the Precambrian gneiss-migmatite complex during incipient rifting as Younger Granites in Nigeria (213 to 141 Ma) [7]. The basement rocks experienced cycles of igneous intrusion during the incipient rifting event after over 400 Ma hiatus. The emplacement of the Younger Granites migrated along ENE-WSW and NNE-SSW lineaments that correspond to the directions of late Pan-African dextral transcurrent faults in the basement parallel to the marginal faults of the Benue Trough, which has been interpreted as a pull-apart basin [8].

The geological evolution of the pegmatites in Nigeria mainly includes "Older Rare-metal Belt" with oxide ore phases from high-temperature reactions in Precambrian times to "Younger Rare-metal Belt" with low-temperature oxide and sulfide ore-association in greisen and veins with Phanerozoic ages [9]. The pegmatite suite is almost exclusively oriented SW-NE from the west around Ilesha and east around the Jos Plateau, cutting western and eastern Nigeria (Figure 1b) [3,5]. Two generations occur around some ring complexes in the Jos Plateau in pegmatitic greisen and veins which formed along reactivated old lineaments by fluids coeval with Mesozoic magma emplacement (Younger Granites) [4,10]. Although most granitic rocks in the Nigerian Younger Granite province (including amphibole-, fayalite-, and biotite-bearing granites) are high in tin, the economic

enrichment of cassiterite and sulfides occurs within biotite granites, greisenized granites, and quartz veins [4].

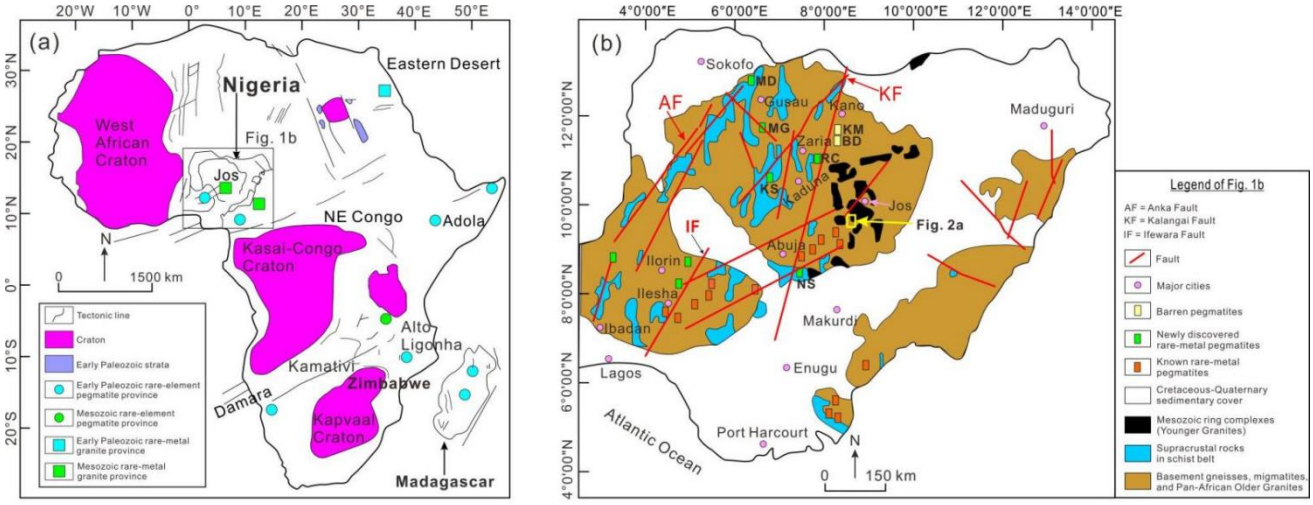

Figure 1. (**a**) Geological sketch map of African rare-element pegmatite and rare-metal granite provinces (Modified after [7,11,12]). Colors indicate age provinces. Box shows the location of Nigerian Precambrian suites and Younger Granites in (**b**); (**b**) Regional geological map of the Nigerian Pan-African basement, showing locations of areas of rare-metal and barren pegmatites.

2.2. Local Geology

2.2.1. Occurrence of Plutons and Mineralization

The study area in the Gindi Akwati region is located within the western edge of the Ropp complex in the Nigerian Younger Granite province. It lies within longitude 9°20′ N to 9°30′ N and latitude 8°50′ E to 8°52′ E at the contact between the Older Granite basement and a Younger Granite intrusive at the western edge of the Ropp anorogenic ring complex (Figure 2a,b). Portions of the Precambrian Older Granites were sheared and greisenized by fluids from Jurassic granitoid intrusions. The marginal greisen strikes nearly N-S and defines a zone of mineralization. The rock types in this area comprise relic gneiss, Older Granite, Younger extrusive relics of volcanic lava and pyroclastics, plutonic suites, and basic dyke swarm. Veinlets in the Older Granites were observed to terminate at the boundary with the diabase dykes, suggesting that the hydrothermal fluids that caused greisenization and veining in the Older Granites occurred before the emplacement of the dolerite dykes.

Stratigraphically, the Precambrian gneisses and Older Granite are the oldest. The earliest phase of Jurassic Younger Granite intrusion was marked by granite porphyry's emplacement, which sheared parts of the Older Granite and mylonitized zone resulted. After that, an intrusion of biotite granite occurred. At late-stage consolidation of the biotite granite, mineralized fluids moved through shears and greisenized marginal parts of country rock (Older Granite). Later, some dolerite dykes intruded along some of the fractures. The Younger Granite magmatism cycle ended with the intrusion of riebeckite-annite granites (Figure 2c).

2.2.2. Deposit Morphology, Alteration, and Ore Mineralogy

Firstly, the ore bodies occur both in the greisenized part of the Older Granite in proximity to short, thin zones of mylonitic rocks and quartz veins. The greisenized parts are related to biotite granite underlying the basement rocks in the relevant marginal zones. Wall rock alteration may occur marginally to the greisenized granites with an increased proportion of quartz, or the veins may infill fissures in the lode system with mineralized

greisenized granite. The greisenized granite, which formed along cooling joints and fractures, is deeply weathered. The grain size of disseminated sulfide and cassiterite in the greisen bodies is about 1 mm. In the past, artisans targeted the primary cassiterite deposits from decomposed greisen around the apical parts of the Older Granite bodies.

The greisenized granites (including ore-bearing and barren ones) are rigorously spatially controlled by faults, such that the length of both the mylonitized zones and altered rocks are nearly identical in places (Figure 2b). Most of the pitting by artisanal miners is along the sheared zones, and their excavations hindered the delineation of the ore bodies' geometry during the present field investigation (Figure 3a). The few greisenized bodies (of about 20 to 35 cm in width) are not continuous and have a dark core that passes gradually (diffuse) into surrounding granite (Figure 3b). In addition, artisans dug pits to explore alluvial cassiterite around a biotite granite outcrop in the vicinity of the Older Granites (Figure 3c,d). A report of core traverses by Ex-Land Company around the Gindi Akwati region shows that several ore greisen zones were intercepted [10]. Their recalculated actual thicknesses from drilled cores range from a few to tens of cm (drill holes: D = 9 to 368 cm and E = 7 to 178 cm) [10]. There are no concise details of tenor, size, shape of ore bodies, or reserves of payable ore in the greisen or quartz veins. The NS-striking ore zones are about 1100 m long and 115 m wide.

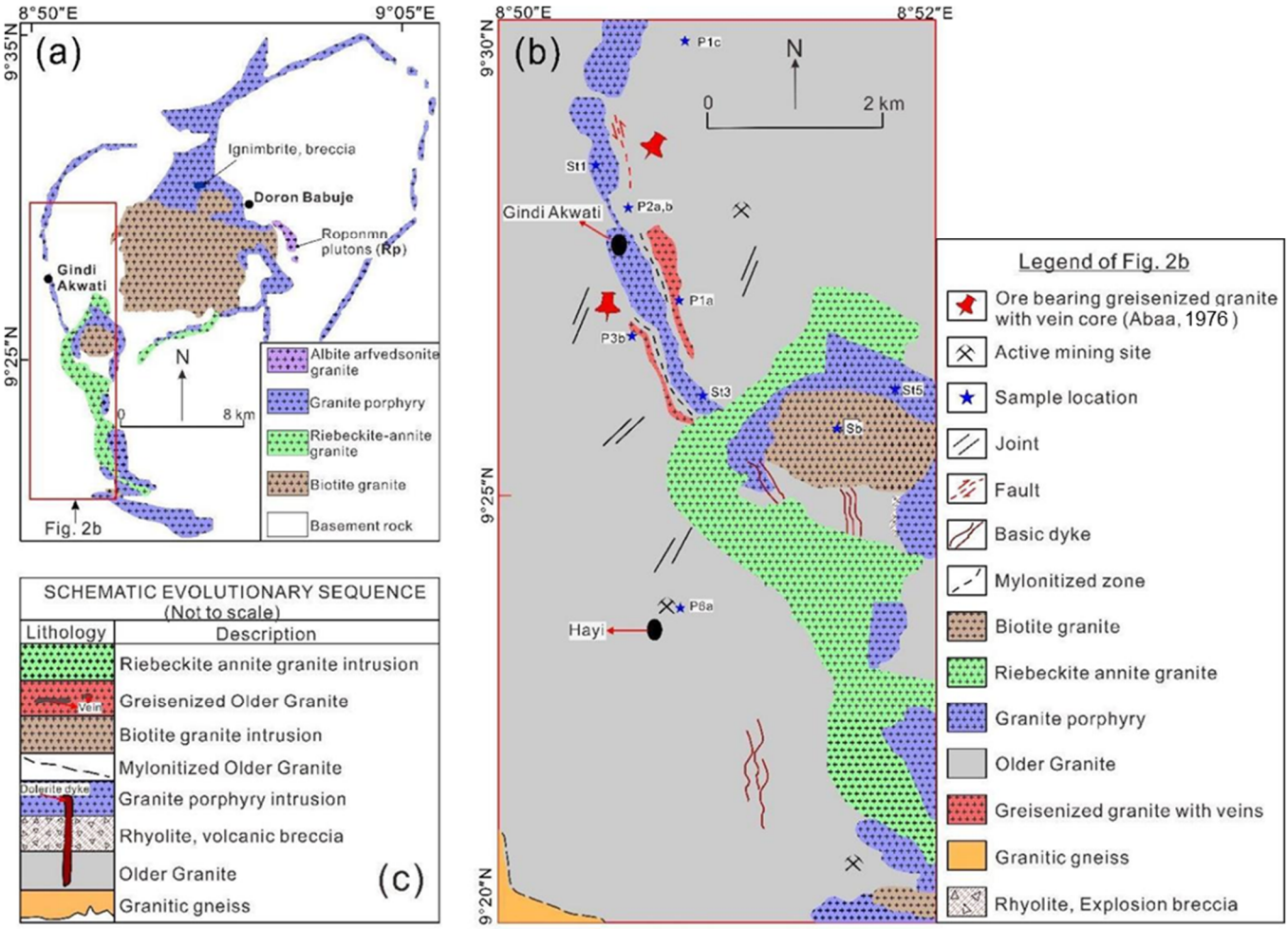

Figure 2. (**a**) Simplified geological map of Ropp Complex showing the distribution of plutons (Modified after [10]); (**b**) Geological map of the western edge of Ropp Complex, where the Gindi Akwati deposit is located; (**c**) Schematic evolution sequence of rocks around the Gindi Akwati deposit, north-central Nigeria.

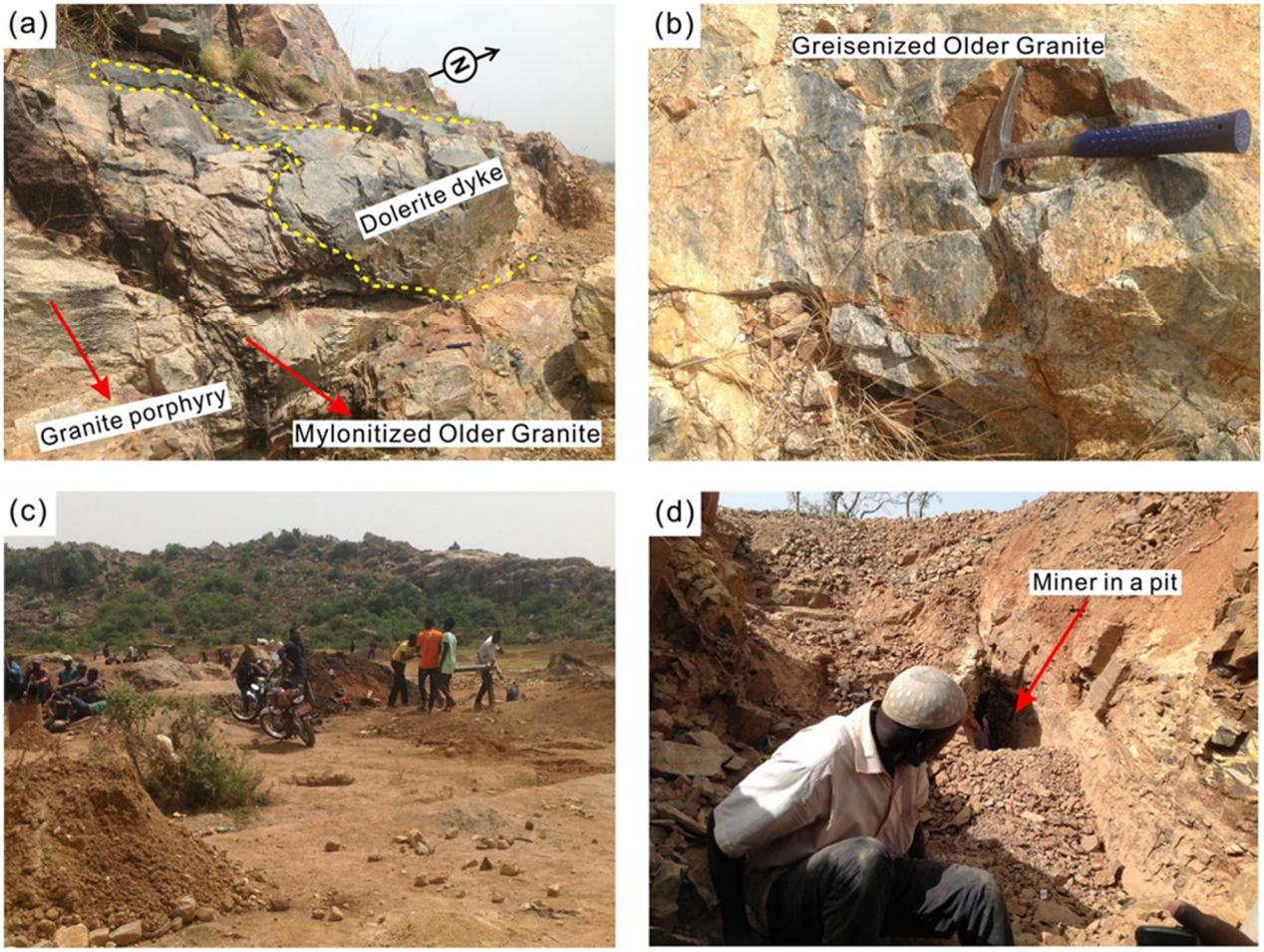

Figure 3. Field photographs that show the contact relationship of igneous rocks and mining scenarios from the Gindi Akwati deposit. (**a**) Contact relation between the Jurassic granite porphyry intrusion (belonging to Younger Granite) and mylonitized Older Granite with dolerite dyke; (**b**) Greisenized Older Granite in the vicinity of the host rock contacted with the granite porphyry; (**c**) Artisanal miners mined alluvial cassiterites close to the roof zone of the biotite granite outcrop; (**d**) Miner dug pits at the marginal contacts (greisenized parts of Older Granite) between the granite porphyry and Older Granite to mine cassiterites in the greisenized granites and quartz veins.

3. Petrographic Characteristics

During this study, we collected twenty-four samples, including six Older Granites, five greisenized granites, eight Younger Granites, and five quartz veins. The characteristic feature of the major mineral assemblages in the Older Granite with its greisenized parts, as well as their accessory mineral phases (Figure 4), granite porphyry, and biotite granite (Figure 5) of the study area, are described herein with the modal compositions (Supplementary Table S1).

3.1. Older Granite, Greisenized Granite, and Quartz Veins

The Older Granites are medium to coarse-grained, light grey, and have black streaks from biotite. They mainly contain quartz, plagioclase, microcline, and biotite, with minor accessory minerals of pyrite, zircon, and titanite (Figure 4). The influx of fluid into parts of the Older Granite changed the texture and altered minerals to form new greisen assemblages (quartz, sericite, topaz, lepidolite, and chlorite). The variations include least altered samples distal to the shear zone, which has an equigranular texture (Figure 4a-c), wall rock to greisenized granite with gneissose foliation (Figure 4d–f), and medium to coarse-grained greisenized granite (Figure 4g–i).

The least altered Older Granite is uniform in texture, mainly containing quartz, plagioclase, microcline, and biotite. The rock is generally granodioritic as the ratio of plagioclase to total feldspar is at least two to one (Supplementary Table S1). The plagioclase has alternating twin lamellae, with inclined extinction (15 to 25 degrees) and cloudy pervasive alteration of some grains (Figure 4b,c). Microcline with tartan twinning occurs interstitially to quartz and plagioclase. Biotites are largely subhedral and equigranular. Pyrite, zircon, and titanite constitute the accessory minerals, and none of the examined Older Granite host rocks contained cassiterite (Supplementary Table S1).

The "Older Granite" wall rock has fine-grained quartz (comminuted), thought to have resulted from its proximity to the shear zone. Some plagioclases show strain effects with bent crystals and twin lamellae. The modal volume of mica, including biotite, chlorite, and muscovite, is higher than the host granite, and some crystals occur as inclusions in feldspars and deformed quartz grains with wavy extinction. Mica grains form elongated fabrics, and their alternation with aligned grains of quartz and feldspars form a gneissose texture. Relics of pyroxene are found within the biotite crystals. Titanite grains cluster to form the main accessory, whereas fluorite, topaz, and pyrite are also important locally (Figure 4e,f; Supplementary Table S1).

The greisenized granite contains minute grains of cassiterite around white to pink feldspars (Figure 4g). The transition from Older Granite to greisen is gradational, increasing white mica from the Older Granite into the greisen (Supplementary Table S1). Mineralizing fluids followed the cataclasis of these rocks, during which time "new" mica (lepidolite) and accessory minerals (fluorite and topaz) were introduced and further replaced the original minerals in the rock. The fine-grained groundmass of quartz, feldspar, and muscovite has some structural alignment (Figure 4h,i). These greisens are topaz-bearing (locally) micaceous quartzofeldspathic rocks that are texturally variable in proximity to the mylonitized zone. The formation of veins and new minerals indicates that recrystallization and hydrothermal fluids induced incipient greisenization. Chlorite, lepidolite, topaz, pyrite, chalcopyrite, and sphalerite constitute accessory phases (Supplementary Table S1).

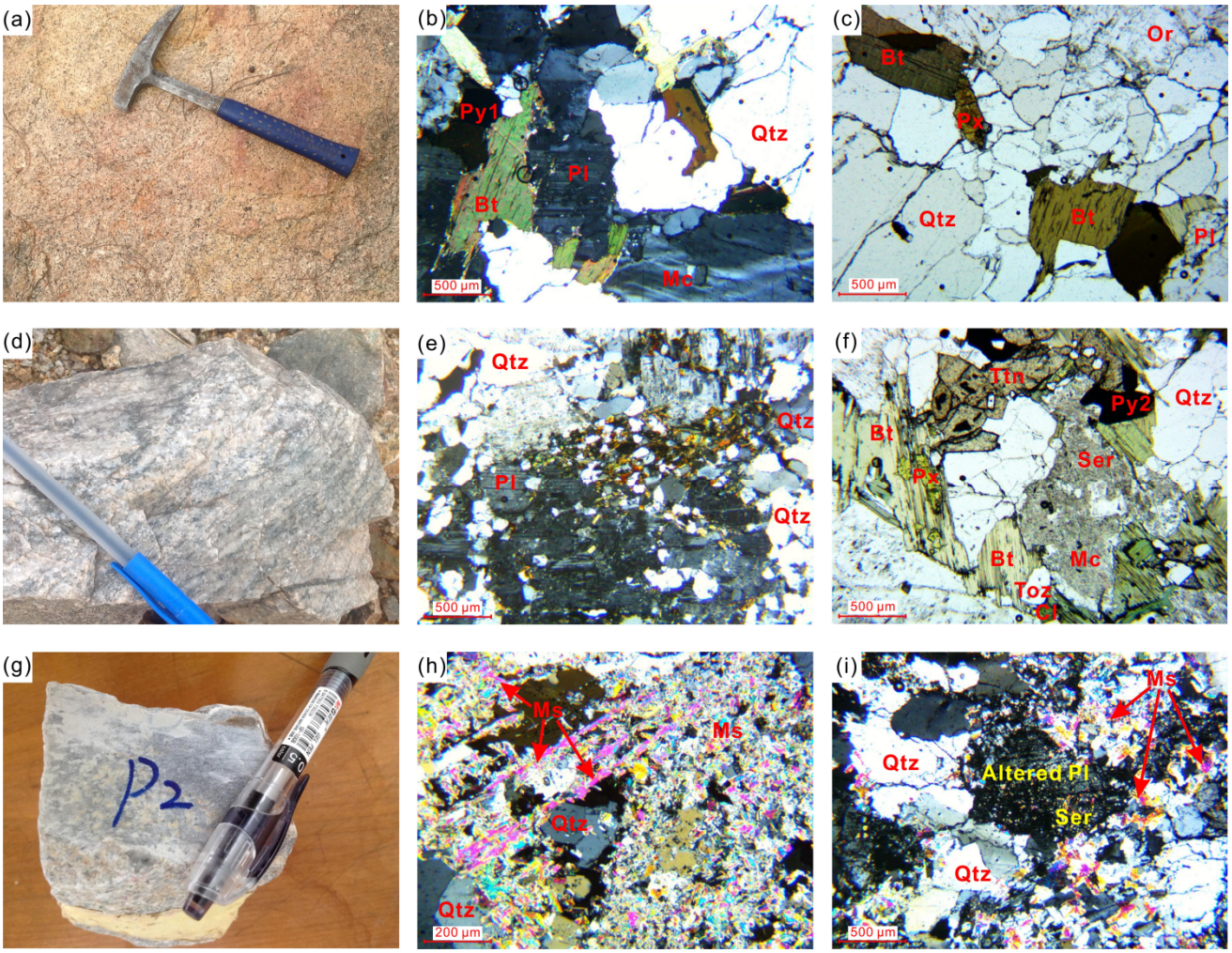

Figure 4. Photographs of hand specimens and microphotographs of Older Granite, greisen wall-rocks, and greisenized granite from the Gindi Akwati deposit. (**a**–**c**) least altered Older Granite; (**d**–**f**) greisen wall-rocks; (**g**–**i**) greisenized granite. Bt = biotite, Cl = chlorite, Mc = microcline, Ms = muscovite, Or = orthoclase, Pl = plagioclase, Px = pyroxene, Py = pyrite, Qtz = quartz, Ser = sericite, Toz = topaz, Ttn = titanite.

3.2. Granite Porphyry

The rock is light grey in color and porphyritic. The phenocrysts consist of quartz, feldspars, and clusters of biotite with specks of iron staining, probably ilmenite (Figure 5a). Some quartz crystals are bipyramidal, and the groundmass is microcrystalline and equigranular. The quartz is microscopically clear, and feldspar is mostly perthitic orthoclase, but dentate albite grows around the rims of some orthoclase crystals (Figure 5b,c). Biotite and pyroxene are the main ferromagnesian minerals. Fluorite and zircon are the main accessory minerals (Supplementary Table S1).

3.3. Biotite granite

The biotite granites are medium to coarse-grained and mainly occur as small circular stocks (Figure 5d). Petrographically, the quartz, and other crystals, are mostly arranged between larger feldspars (Figure 5e). The feldspars are usually soda-rich plagioclases (albite), K-feldspars (orthoclase, microcline), and perthites. The modal albite is similar to those of K-feldspars (Supplementary Table S1). There are two generations of albite, including polysynthetically twinned albite, mostly altered to sericite and small crystals of deuteric albite (Figure 5e). The quartz is mainly clear, but some grains displayed wavy extinction. Biotite and hornblende are the main ferromagnesian minerals, and they are

locally highly altered due to pervasive metasomatism (Figure 5f). Epidote, opaque oxides, fluorite, and zircon are the main accessory minerals (Supplementary Table S1). The biotite granite shows good consistency in mineral composition and texture.

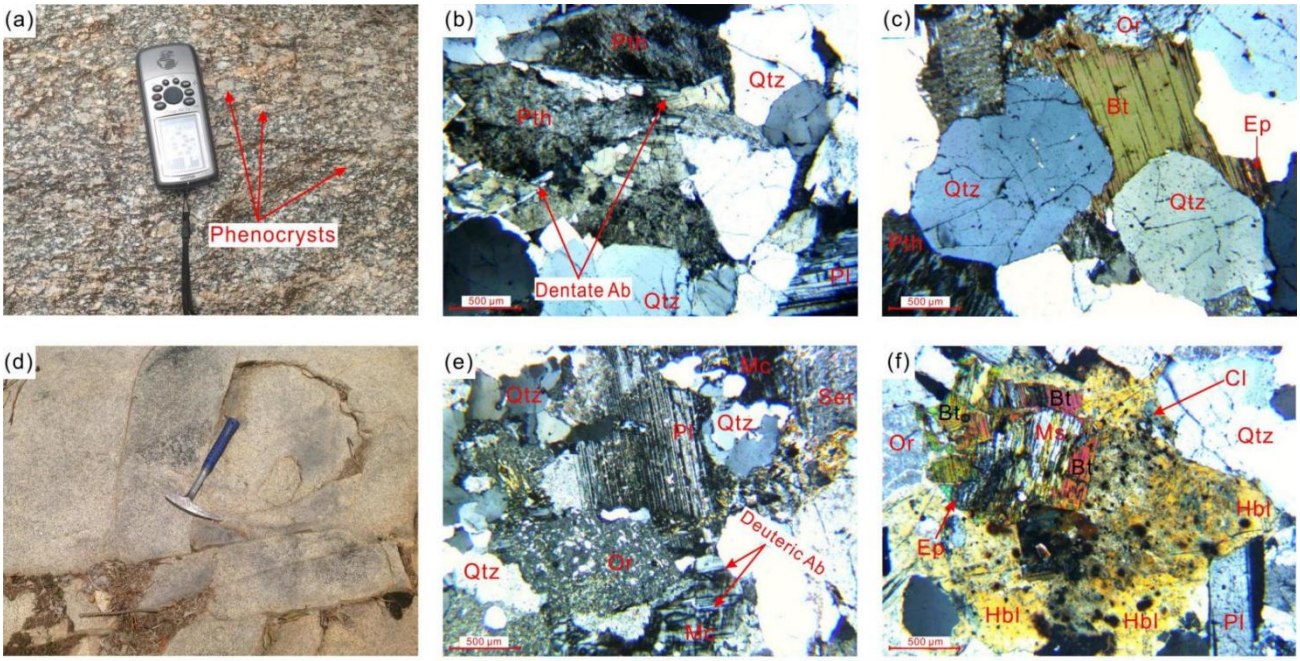

Figure 5. Photographs of hand specimens and microphotographs of Younger Granite (YG, including granite porphyry and biotite granite) from the Gindi Akwati deposit. (**a**–**c**) granite porphyry; (**d**–**f**) biotite granite. Ab = albite, Ep = epidote, Hbl = hornblende, Pth = perthite.

3.4. Ore Microscopy

The distribution of mineralization is structurally controlled, contained in mylonitized zones that are locally greisenized (micaceous quartz-feldspar veins) around the Gindi Akwati region. In the weathered parts (down to a depth of about 6m), the ore mineral in order of abundance is cassiterite (SnO_2), chalcopyrite ($CuFeS_2$), and sphalerite (ZnS). Pyrites (FeS_2) are significant locally (Figure 6). In some greisenized granites, chalcopyrite and cassiterite are mainly associated with lepidolite (Li-mica). Topaz and fluorite occur in trace amounts (Supplementary Table S1). The core samples that were taken at a greater depth (drill holes D and E; > 40 m) around the Gindi Akwati region had massive brown and grey sphalerite as the main ore in the greisenized granites and quartz veins. The other sulfides and cassiterite are subordinate in abundance [10].

The disseminated mm-sized crystals of pyrite (Py1) in Older Granite are thought to be magmatic relative to the crystallization of host rock, whereas the other larger pyrite grains (Py2) in the greisenized, quartz vein probably co-crystallized with other sulfides and cassiterite during late-stage consolidation of Younger Granite intrusive (Figure 6b). The veins are oriented parallel to the long axis of these greisens within the host rock. The tectonic process that produced the foliation in the greisenized parts of the host rock may be syngenetic with these parallel veins. There are multiple generations of hydrothermal fluid-induced recrystallization, mineralization, or at least variable conditions during crystallization from the parental fluid. The first fluids were more enriched in cassiterite and occurred along with feldspars alteration after shearing in the Older Granite (Figure 6e). Late-stage silica metasomatism deposited Cu-Zn-Fe sulfides intimately connected with partly zoned Li-mica (Figure 6f). Similar patterns have been reported in other complexes, but cassiterite's main ore occurs in two forms: disseminations and greisen veins [3].

The color and pleochroism of cassiterite differ between various types of occurrence/paragenesis; these grains in the greisens are colorless to white without distinct zoning (Figure 6e), whereas the crystals from quartz veins display two zoning styles: oscillatory zoning and sector zoning (Figure 6k). The oscillatory zoned crystal has successive alternating zones of colorless, white, yellow, orange, and deep reddish-brown zones. The zone boundaries are usually planar and parallel to crystallographic growth planes (c-axis) (Figure 6k). The zones may be discontinuous due to a change in nucleation conditions.

The close association of Li-mica and fluorite with cassiterite (Figure 6e,f) suggests a genetic link between their formation and tin precipitation, which may be related to the mineralizing fluid (e.g., [13]). The irregular contact at the mineral boundaries between individual massive, unstrained quartz crystals, and their sub-grains suggests low-temperature grain boundary migration associated with mineralizing hydrothermal fluids. Ore texture includes: (a) euhedral granular (Figure 6b), subhedral-anhedral granular (Figure 6e,h), poikilitic, exsolution texture (Figure 6b,i); (b) metasomatic, radiating fibrous (Figure 6e,f), lattice filling textures (Figure 6h,l); and (c) rim texture with gangue replacing chalcopyrite (Figure 6i).

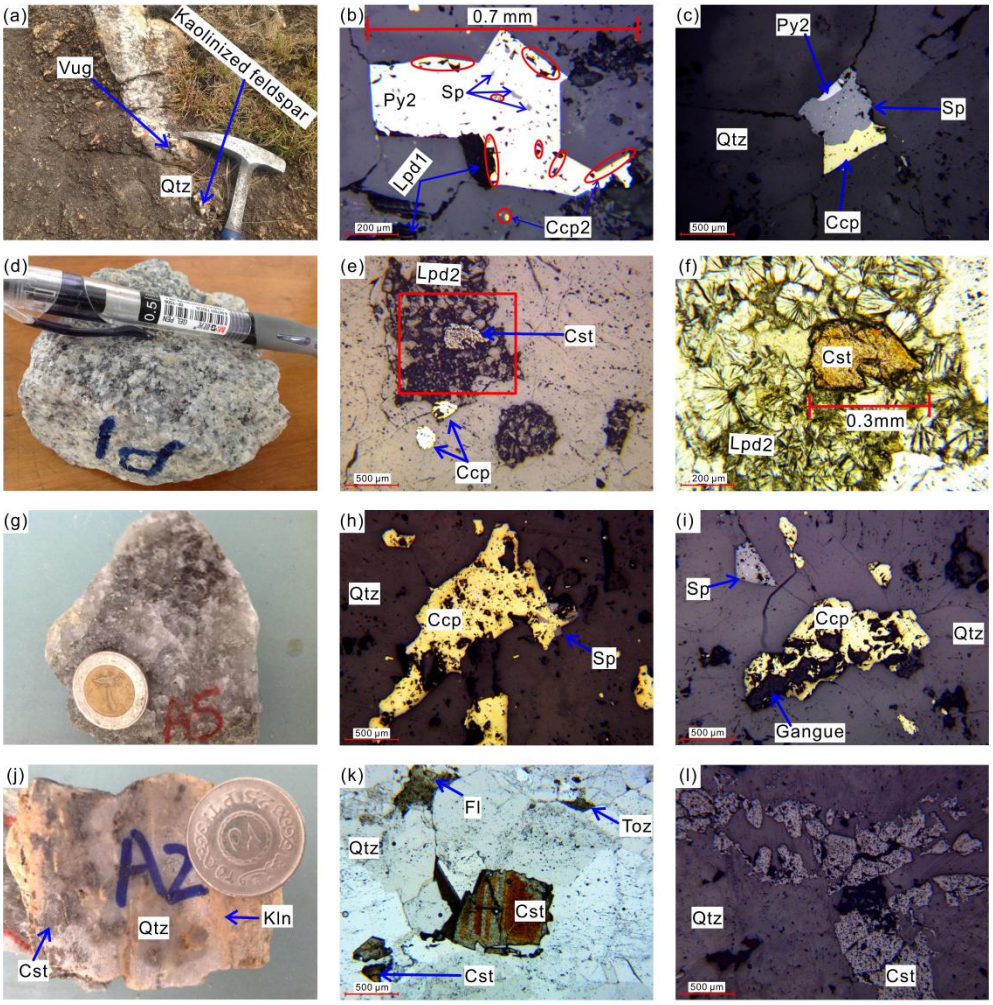

Figure 6. Field photograph, hand specimens, and microphotographs of mineralized rocks from the Gindi Akwati deposit. (**a**) quartz vein with vugs and kaolinized feldspar in greisenized granite; (**b**) typical oxidation halos around lepidolite; (**c**) euhedral granular sulfides co-precipitated; (**d**,**e**) greisenized granite containing co-existing cassiterite and chalcopyrite; (**f**) magnified view showing comb textured lepidolite; (**g**) contact between the ore-bearing vein and greisenized granite; (**h**,**i**) chalcopyrite with sphalerite rim, fine corrosive inclusions and chalcopyrite cut by replacive gangue; (**j**–**l**) pseudo-alignment of cassiterite grains, alteration of feldspar to kaolin and accessory fluorite

and topaz. Ccp = chalcopyrite, Cst = cassiterite, Fl = fluorite, Kln = kaolinite, Lpd = lepidolite, Py = pyrite, Qtz = quartz, Sp = sphalerite, Toz = topaz.

4. Analytical Methods

4.1. Whole-Rock Major and Trace Element Analysis

Major elements and trace elements (including rare earth elements (REE)) were analyzed in the ALS Laboratory Group in Guangzhou. Six granite samples were subjected to appropriate pre-treatment including pulverization with an agate ball mill to <200 mesh size. Loss on ignition (LOI) was determined after igniting the sample powders at 1000°C for about one hour. Major element contents were analyzed using a PAN analytical Axios X-ray fluorescence (XRF) spectrometry. Detailed analytical methods were described by Liu et al. [14]. The analytical uncertainties were better than 1%, with analytical precisions as follows: SiO_2: 0.8%; Al_2O_3: 0.5%; Fe_2O_3: 0.4%; MgO: 0.4%; CaO: 0.6%; Na_2O: 0.3%; K_2O: 0.4%; MnO: 0.7%; TiO_2: 0.9%; and P_2O_5: 0.8%. The trace element concentrations (including REE) were analyzed using an inductively coupled plasma–mass spectrometry (ICP-MS), with a Finnigan MAT Element II mass spectrometer. Before being analyzed, the samples were put in Teflon screw-cap bombs for 2-day closed beaker digestion using a mixture of HF and HNO_3 acids, and then the dissolved samples were diluted to 80 g with 2% HNO_3 prior to the analysis. The analytical precision was generally better than 5% (2σ).

4.2. Electron Probe Microanalysis (EPMA)

Major element compositions of cassiterite were analyzed using a SHIMADZU–1600 coupled with an energy dispersive spectrometer at the Chinese Academy of Science (CAS) Key Laboratory of Crust-Mantle Materials and Environmental Sciences at the University of Science and Technology of China (USTC). For the analysis of cassiterites, an accelerating voltage of 15 kV, beam size of 1 μm, and a low beam current of 0.01 μA was used. A program based on the ZAF procedure was applied for matrix correction.

4.3. In Situ LA-MC-ICP-MS Analysis of Sulfur Isotope

In situ sulfur isotopes of sulfides in thin sections were analyzed using a Nu Plasma 1700 multiple-collector inductively coupled plasma mass spectrometer (MC-ICP-MS) configured with a RESOlution M-50 excimer ArF laser ablation system (LA) at the State Key Laboratory of Continental Dynamics, Northwest University, Xi'an, China. Sulfur isotopes of ten sulfide samples (including four chalcopyrites, three pyrites, and three sphalerites) were obtained. The diameter of the laser beam was set to 25–37 μm under the condition of the energy density of 3.6 J/cm^2 and a frequency of 3 Hz, with He gas as the carrier gas during the analytical process [15]. The data correction method employed the sample-standard bracketing method (SSB) and the standard sample for the calibration included IAEA-S-1, IAEA-S-2, and IAEA-S-3 (Ag_2S powder). The in-house sulfur reference material (Py-4, $\delta^{34}S_{V\text{-}CDT}$ = 1.7 ± 0.3‰) with better homogeneity was used for external standard bracketing, and it was tested every eight samples [16]. Detailed analytical methods were described by Chen et al. [17] and Yuan et al. [18]. The analytical precision (1σ) is ± 0.1‰. The sulfur isotope ratios are expressed in terms of permil (‰) and are reported using delta notation ($\delta^{34}S$) relative to the Vienna Canyon Diablo Troilite (V-CDT) standard: $\delta^{34}S_{V\text{-}CDT} = [(^{34}S/^{32}S_{sample}/^{34}S/^{32}S_{V\text{-}CDT}) - 1] \times 1000$ [18].

4.4. Fluid Inclusion Analysis

Sixty-six inclusions from cassiterite- and sulfides-bearing quartz veins were analyzed during this study. Microthermometric analyses were carried out at the Fluid Inclusion Laboratory of the Chinese Academy of Science (CAS), Key Laboratory of Crust-Mantle Materials and Environmental Sciences, University of Science and Technology of China (USTC). These inclusions were from nine doubly polished wafers and were chosen under the microscope. The microthermometric analysis was conducted on a Linkam THMSG600

heating-freezing stage. The precision was ±1 °C and the temperature range is from -196 to +600 °C. The temperature was calibrated using Synflinc synthetic fluid inclusion standards (USGS). Detailed analytical methods of the freezing point, the formula of a freezing point drop in temperature, and salinity of aqueous inclusions salinity were described by Bodnar [19].

5. Results

5.1. Geochemical Characteristics of Gindi Akwati Granites

Whole-rock major and trace element contents of Older Granite country rock (n = 6; with 3 samples each from the north and south of the Gindi Akwati region), weakly greisenized parts of Older Granite (n = 5), and Younger Granite (biotite granite and granite porphyry) in their vicinity (n = 8) from the Gindi Akwati region are given in Supplementary Table S2. The SiO_2 in the host rock and Younger Granites are high (>70 wt. %) except for two greisenized granites with lower contents (P2a = 68.89 and P6a = 67.35 wt. %). The increase in silica indicates the edging of granites more toward the acidic front. Because alterations are known to accompany greisenization, constraints from immobile elements are used to classify the greisenized granite. Some greisenized granites are plotted in the field of granodiorite in the diagram of Zr/TiO_2 versus Nb/Y, according to Vry et al. [20] and Winchester and Floyd [21] (Figure 7a). Comparison with mobile element data displays that all the Younger Granites and the greisenized zones are markedly enriched in K_2O (Figure 7b), confirming the igneous matrix's intense potassic alteration (microclinization). In addition, the SiO_2 contents of the greisenized granite plot in the granodiorite field are slightly lower than those of Older Granite. This indicates that some silica loss occurred during greisen alteration (e.g., [22]).

The host rock (Older Granite) and Younger Granite are weakly peraluminous (A/CNK <1.2) (Figure 7c) with low TiO_2 and P_2O_5 contents. The contents of CaO are higher in the host rock (Older Granite) (average = 1.27 wt. %) than in the Younger Granites (average = 0.56 wt. %). Other ferromagnesian constituents, including MgO (average = 0.01 wt. %), MnO (average = 0.01 wt. %) and FeO^T (average = 1.38 wt. %) in the biotite granites, are lower than most known granites. In the biotite granites, the ratios of FeO^T/MgO (range = 62–168) and FeO^T/MnO (range = 80.5–124) are systematically strongly anomalous to the mean values of the upper continental crust (2.0 and 50.4, respectively [23]). Tin-bearing granites have higher contents of SiO_2 and K_2O and lower contents of TiO_2, FeO^T, MgO, and CaO [24]. The trend of a near reciprocal relationship between mafic and felsic constituents, which is famous in tin-bearing granites globally, occurs in the Younger Granites (Figure 7d). The inverse relations of Na_2O and K_2O (r = −0.81) with respect to silica variation reduced their correlation (r = −0.87).

The contents of trace elements in tin-bearing biotite granites deviate markedly from the Older Granites of the Gindi Akwati region. The greisenized (topaz-bearing) portions of the Older Granite, on the other hand, mirrored some of the biotite granite's characteristics, such as REE and other trace element concentration and fractionation. The biotite granites are characterized by a high content of Ga (63.9–81.9 ppm), Nb (118–162 ppm), Rb (495–705 ppm), Ta (21.9–32.1 ppm), Th (41.0–64.7 ppm), and Y (152–236 ppm) and low contents of Ba (41.9–89.5ppm), Sr (14.7–39.5 ppm), and Zr (100–300 ppm) (Supplementary Table S2). The variety of accessory minerals, high DI (92–96), and low K/Rb ratios in the Younger Granites (biotite granite = 52–82, granite porphyry = 78–136) is typical of highly differentiated granites. The ternary Rb-Ba-Sr plot confirms that the Younger Granites are strongly differentiated [25] (Figure 7e).

The contents of Sn in Older Granites (3–7 ppm) are typically around the bulk crustal values of 3–5 ppm Sn [26], whereas the contents are a bit elevated in the greisenized granite (9.00–40.0 ppm). Generally, the background contents of Sn in "barren" granites from the Nigerian Younger Granite province (average Sn = 30 ppm; [27]) are multiples higher than average abundance in the continental crust; 3–5 ppm of Clarke. The mean value of

20 ppm from granite porphyry is much lower than those of the Nigerian Younger Granite province. However, biotite granites have a larger variation in Sn content (range= 88.0–189 ppm) than barren granites and granite porphyry. The mean ratios of Nb/Ta (range = 4.81–6.18) and Zr/Hf (range = 8.35–30.81) of elements with similar chemical behavior of the Younger Granite also deviate from the usual crustal values (11 and 33, respectively; [28]). Furthermore, low Nb/Ta ratios of 3.42 and 5.27 occur in two greisenized granites (Figure 7f, Supplementary Table S2).

There is strong parallelism in enrichment and depletions in the Younger Granites (biotite granite and granite porphyry). The shape of the spider diagram of trace elements normalized to the upper continental crust shows enrichment of large ion lithophile elements (LILE) and some high field strength elements (HFSE) in the Younger Granites [28]. In addition, it shows negative anomalies of Ba, Sr, P, and Ti (Figure 8a). The total REE contents are consistently higher in the biotite granite plutons (∑REE = 300–371 ppm, average = 344 ppm) than in the granite porphyry (∑REE = 149–156 ppm; average = 146 ppm) from the Gindi Akwati region. However, the total REE contents are lowest in the host rock of Older Granite (∑REE = 132–152 ppm; average = 142 ppm) (Supplementary Table S2). In terms of REE concentrations, fractionation patterns, and Eu anomalies, the rocks show a lot of variation. They also have higher light REE content than heavy REE (Supplementary Table S2), and chondrite-normalized patterns show significant LREE enrichment (Figure 8b). The greisenized parts of Older Granites have higher REE contents (198–260 ppm; average = 217 ppm) compared with the least altered Older Granite (Supplementary Table S2) and have chondrite-normalized patterns nearly parallel to those of the biotite granite (Figure 8b).

5.2. Mass Changes During Greisenization

The mean chemical contents of the least altered Older Granite and associated altered rocks were used to investigate losses and gains during greisenization. The data scatter from the isocon diagram indicates that the major and trace elements were mobile to varying degrees (Figure 9a,b). The best fit isocon (blue equiline; Figure 9a) for the altered granite is defined using linear regression of the presumably least scattered of all elements (Al and Si), assuming that these elements were immobile during greisenization (e.g., [2]). The aluminum immobility is a reasonable assumption considering that feldspars are replaced by muscovite, which is a major aluminum-bearing mineral.

Because of the large scale of the isocon plot, some elements that clustered close to the isocon may appear to lie above (enriched) or below it incorrectly (depleted) [29]. As a result, mass change was calculated by clustering slopes to datapoints, identifying elements with similar behavior and averaging the slopes for the selected presumably immobile species at unity (Figure 9b). Generally, the whole-rock mass balance changes are expressed by the loss of Si, Ca, Ti, Cs, Ba, and Sr and the enrichment in Rb, Nb, Ta, U, Th, Ga, Zr, Hf, Sn, W, Y, Fe, P, Mn, and ∑REE. The enrichment and depletions peculiar to the altered variants are reconcilable with the mineralogical changes. For example, depletion of Ba and Sr could be due to feldspar dissolution in the greisenized granite. Furthermore, elements hosted by accessory zircon and apatite (such as P, Zr, Th, and Y) become partially enriched during greisenization [2,30].

Chemical alteration index (AI), [AI = $Al_2O_3/(Al_2O_3 + CaO + Na_2O + K_2O) \times 100$], suggests a relatively low degree of alteration (AI = 58.8–65.9 %, Supplementary Table S2) involving breakdown of feldspars (e.g., [31]). The relatively low scatter of major and trace elements in the isocon plots suggests depletion and enrichment trends typical for weakly greisenized granites associated with mineralization (e.g., [2]).

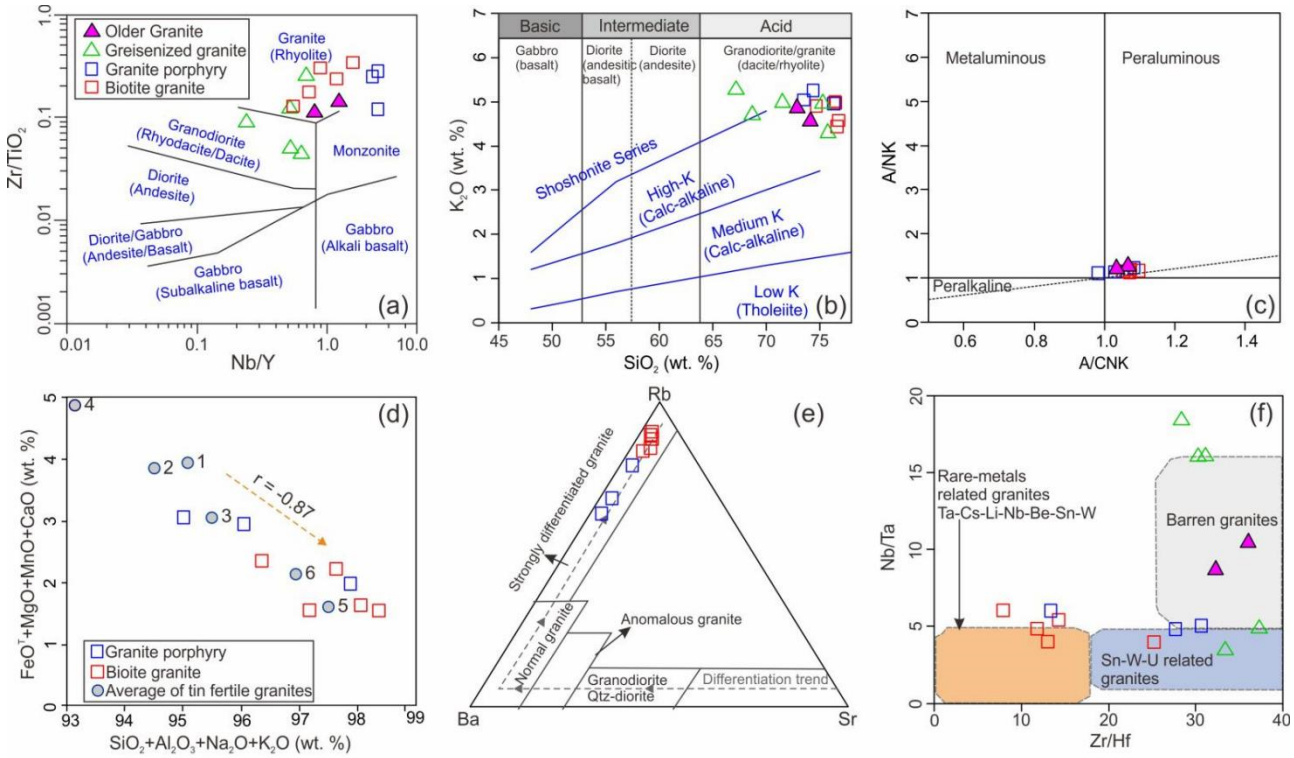

Figure 7. Classification and discrimination diagrams for Older Granite, greisenized granite, and Younger Granite (including granite porphyry and biotite granite) from the Gindi Akwati deposit. (**a**) Zr/TiO_2 vs. Nb/Y diagram following the classification of Vry et al. [20], as modified from the classification diagram for volcanic rocks of Winchester and Floyd [21]; (**b**) SiO_2 vs. K_2O binary plot that covered dispersion from potassic alteration following the classification of Vry et al. [20], as modified from classification diagram of Peccerillo and Taylor [32]; (**c**) ASI vs. A/NK diagram (after [33]); (**d**) Binary variations between acidic (SiO_2 + Al_2O_3 + Na_2O + K_2O) and mafic (FeO^T + MgO + MnO + CaO) constituents of tin fertile granitic rocks (after [24]). Orange dashed arrow represents the trend of correlation of major elements. The r value shows the correlation coefficient. 1 = Malaysia, 2 = Cornwall, 3 = Tasmania, 4 = Bushveld, 5 = Alaska, 6 = Nigeria; (**e**) Diagram of Rb-Ba-Sr (after [25]) which shows the granite porphyry and biotite granite are strongly differentiated; (**f**) Diagram of Nb/Ta vs. Zr/Hf (after [34]). The Older Granite and greisenized granite mainly plot in the area of barren granites, whereas granite porphyry and biotite granite mainly plot in the area of rare-metals-related granites (Ta-Cs-Li-Nb-Be-Sn-W) and Sn-W-U related granites.

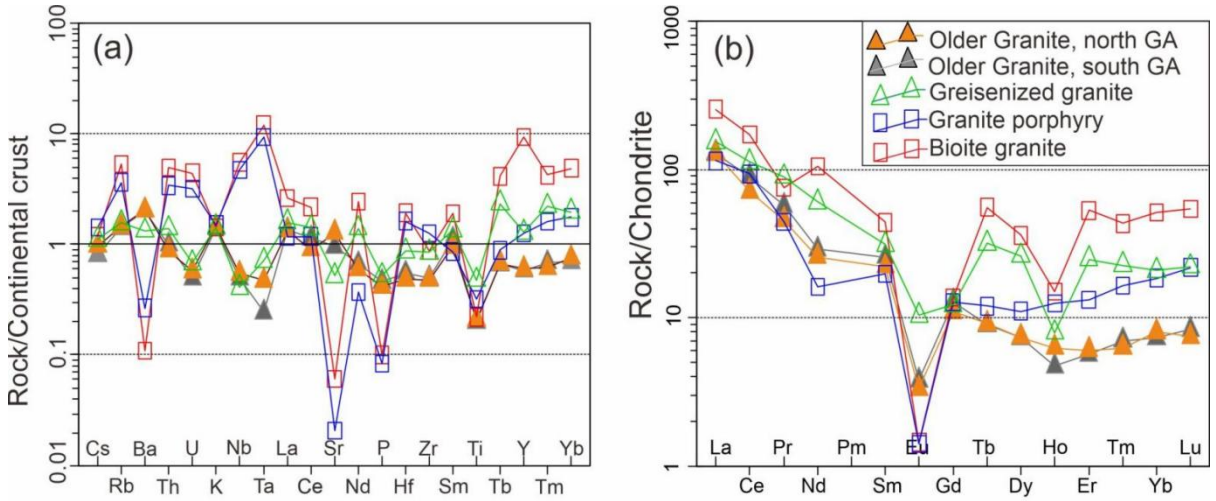

Figure 8. Distributions of trace elements and REE of the Older Granite, greisenized granite, and Younger Granite (including granite porphyry and biotite granite) from the Gindi Akwati deposit.

(**a**) Spider diagrams of trace elements, Upper Continental Crust is according to [28]; (**b**) Chondrite-normalized REE distribution patterns, Chondrite is according to [35].

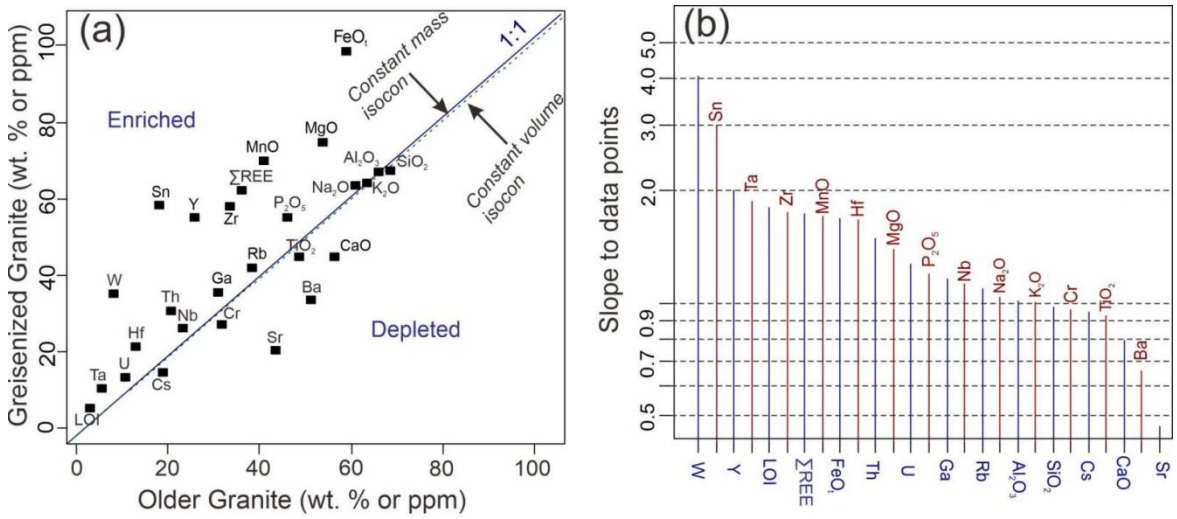

Figure 9. Isocon analysis of the host Older Granite vs. Greisenized granite from the Gindi Akwati deposit. (**a**) Isocon diagram. The element contents of Older Granite and greisenized granite use the average value of samples analyzed in this study (according to [36]); (**b**) Clustering slopes of elements for the selected, presumably immobile, species (according to [29]).

5.3. Hydrothermal Alteration and Mineral Paragenesis

Structurally, the joints and fissures from the cataclasis of Older Granite opened a pathway for fluids that modified the host rock in the vicinity. The petrological changes are limited to narrow zones, although the degree of reactions may be locally intense, depending on the intensity of previous sodic or potassic metasomatism [3,37]. Based on mineralogy and whole-rock chemistry signatures, muscovite enrichment is closely associated with cassiterite and sulfide in greisens (Figure 5e,f), which could indicate the interaction of the ore fluid with biotite-rich wall rocks, resulting in the formation of muscovite (muscovitization) and quartz (e.g., [38]). Thus, the fluids locally react with and mineralize the host rock. During this time, topaz, fluorite, and lepidolite (lithium-rich muscovite) were introduced, and the original minerals of the Older Granite were altered or replaced to form a dark-colored fine-grained matrix (greisen assemblages) with feldspars transforming into microcline (K-metasomatism).

After that, acid metasomatism triggered hydrolysis reactions that produced hydrous minerals from anhydrous phases in response to changes in K^+/H^+ in the fluid, resulting in a classic greisen assemblage of sericite-topaz-quartz [3]. Subsequently, propylitic alteration transformed perthitic feldspar into light grey colored micaceous aggregates and biotite to chlorite. Fluoridization accompanies chloritization and aids the transport and deposition of sulfides. In addition, the fissure-filling veins are thought to locally increase quartz modal content in the rock around their vicinity. This caused silica metasomatism to be associated with the deposition of some sulfides. Finally, the late-stage argillic alteration process leads to kaolin formation at the expense of the feldspars in the greisenized granite and quartzofeldspathic veins [38].

The last stage is highly mobile, where solutions travel upward, resulting in the emplacement of mineralized quartz and muscovite lodes in the greisenized portions of the Older Granite pluton. This trend is similar to that reported for McConnochie greisenized granite and lode veins in Westland, New Zealand [39]. The relative variability of ore abundances from the surface (present study) and cores at depths of about 40 m may reflect the effect of hydrothermal fluid pulses, temperature and pressure changes, and probable variability in alteration of the marginal parts of the Older Granites [10]. Therefore, the primary mineral associations of the host rock and mineralized greisens reflect the dominant

open system processes around the Gindi Akwati region. The mineral assemblages from the altered rocks include two groups, one group including quartz, feldspar, mica, fluorite, pyrite, chalcopyrite, and the other group including topaz, and quartz, feldspar, mica, cassiterite, chalcopyrite, and sphalerite (Figure 10). The distribution of greisenized portions of Older Granite containing ore-bearing quartz veins defined the zone of mineralization.

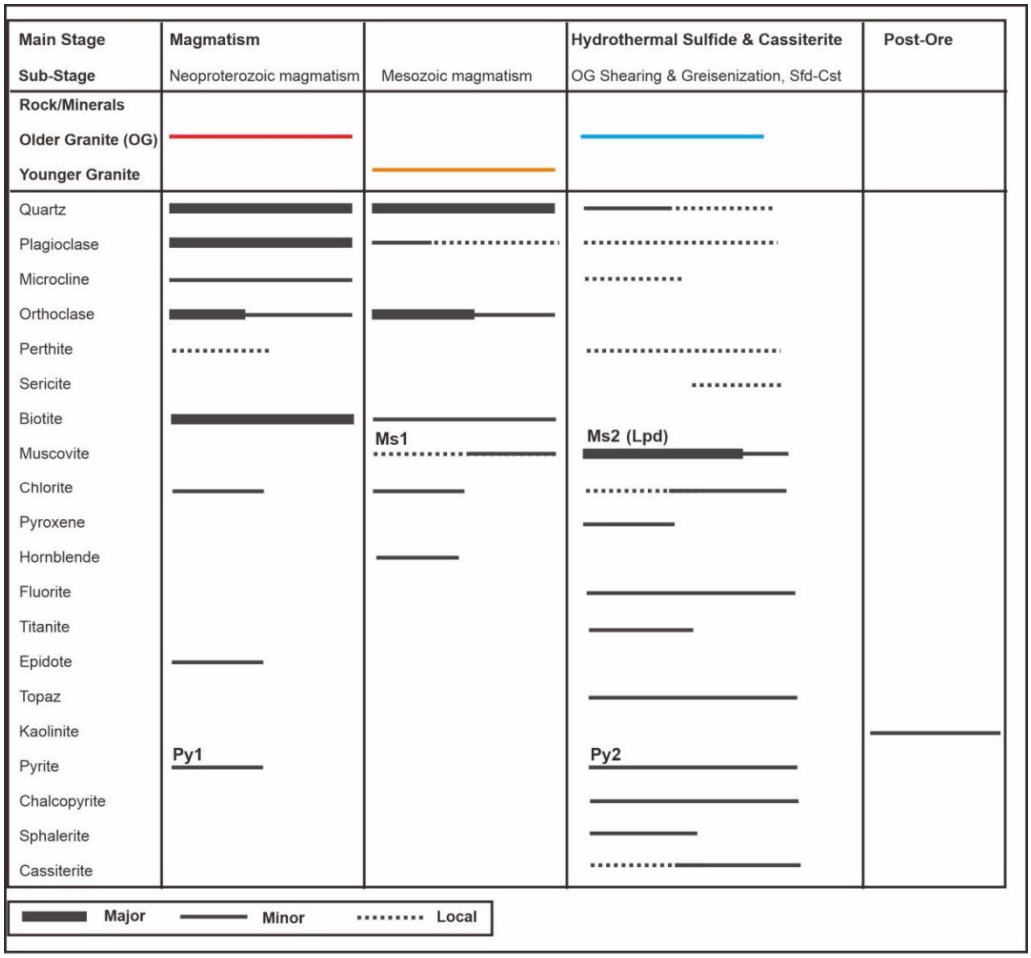

Figure 10. The simplified paragenetic sequence of the mineralized zone from the Gindi Akwati deposit is interpreted from texture, reflected and transmitted light microscopy, and alteration patterns. The bold lines indicate high abundance, the thin lines represent minor amounts, and the dashed lines indicate the local occurrence of trace amounts of uncertainty in determining the paragenetic sequence due to the lack of a clear textural relationship.

5.4. Ore Mineral Chemistry and Sulfur Isotopes

The analyses include discrete grains traversing across (core to rim) granular masses of cassiterite. The results for cassiterite are presented in Supplementary Table S3.

5.4.1. Cassiterite

The chemical composition of cassiterite in the greisen granite and quartz veins ranges from near to ideal SnO_2 (97.10 to 99.28 wt. %). The contents (wt. %) of important minor elements Ti, Ta, Nb, and W are generally higher in the quartz veins than in the greisen, except for Fe. The cassiterite in the greisen granite and quartz veins include TiO_2 (0-0.88 wt. %), FeO (0–0.71 wt. %), and WO_3 (0–0.99 wt. %). Contents of MnO (0–0.04 wt. %), Ta_2O_5 (0-0.18 wt. %), and Nb_2O_5 (0–0.51 wt. %) are much lower and mainly below detection limits in the greisenized granite (Supplementary Table S3). These are similar to trends reported for Hub stock greisen from the Czech Republic [2].

The Ta and Nb contents in greisenized granite are erratic without a clear pattern, as some are below the detection limit. In quartz veins, light zones are more enriched in Nb and Fe than darker zones, which are enriched in Ta (with Nb_2O_5/Ta_2O_5 ratios, ranging between 1.75 and 7.06) (Supplementary Table S3). The contents of Nb, Ta, and W in quartz veins and greisen (few above detection limit) generally decrease with SnO_2 (Quartz vein, $r^2 = -0.56$, −0.68, and −0.95; Greisen granite, $r^2 = -0.13$, −0.53, and −0.70, respectively) (Figure 11a-c). In addition, Ti content slightly increases with SnO_2 ($r^2 = 0.50$ and 0.47 in quartz vein and greisen, respectively) (Figure 11d). This, coupled with a lack of correlation in content of Fe and W in the greisen granite and quartz vein, mimics its complex internal zoning from them and other elements with trace level substitutions for Sn [40]. The most plausible record is the detection of an appreciable amount of W that is usually substituting for Sn of the cassiterite structure in greisenized granites ($r^2 = -0.70$) and quartz veins ($r^2 = -0.95$) (Figure 11c). They are granite-related Sn deposits (Figure 11e) with quadrivalent Sn 2:1 coupled substitution mechanism dominating (Figure 11f).

5.4.2. Sulfur Isotopic Compositions

The MC-ICP-MS in situ sulfur isotopic ($\delta^{34}S$) data of ten sulfide minerals from quartz veins and greisenized granites are listed in Supplementary Table S4 and plotted in Figure 12. During the ore-forming stage in the study area, the sulfides produced are mainly chalcopyrite, sphalerite, and pyrite.

The sulfides have $\delta^{34}S_{V\text{-}CDT}$ values ranging from −1.30 to +0.87‰, with an average value of −0.13‰ (Supplementary Table S4). These values are consistent with the restricted range for co-existing sulfide assemblages (chalcopyrite, molybdenite, galena, sphalerite, and pyrite) in granite and quartz veins in Nigeria (with $\delta^{34}S_{V\text{-}CDT}$ values from 1.44 to +1.75‰) [41] and for I-type granites in Western Carpathians, Slovakia (with $\delta^{34}S_{V\text{-}CDT}$ values from -2.9 to +2.3‰, average = −0.7 ± 1.9‰; Figure 12) [42]. Higher $\delta^{34}S_{V\text{-}CDT}$ values were reported from sulfides in gold-bearing quartz veins in the Anka Schist belt (from 1.9 to 7.8‰) [43], Bin Yauri (from 1.5 to 9.4‰) [44] in NW Nigeria, and barite mineralization in the Benue Trough (from 12.3 to 13.1‰) in NE Nigeria (Figure 12) [45].

The sulfur isotope composition ($\delta^{34}S_{H2S}$) was calculated using the equation: $\delta^{34}S_{H2S} = \delta^{34}S_i - A_i \times (10^6 \times T^{-2})$, where i represents different sulfides; A_i values are 0.40 for pyrite, 0.10 for sphalerite, and −0.05 for chalcopyrite [42]; and T represents the average homogenization temperatures of fluid inclusions (257.6 °C). Thus, the calculated $\delta^{34}S_{H2S}$ values of the fluids are from −1.93 to 0.51‰, with an average of −0.49‰.

5.5. Fluid Inclusion Petrography and Microthermometry

The details of individual inclusion data are given in Supplementary Table S5. A summary of fluid inclusion data for the quartz veins from the Gindi Akwati deposit is provided in Supplementary Table S6 and Figure 13. Many of the inclusions from quartz veins bearing cassiterite are too small (<5 μm) for measurements, except for a few, where seventeen (17) measurements were taken. The inclusions' morphology varies from ovoid to ellipsoid through tubular to highly irregular and some contain halite (Figure 13a). As the eutectic point for the NaCl-H_2O system (i.e., –20.8 °C) was not reached, the freezing point temperature (Tm_{ice}) for these inclusions allows a relatively accurate determination of salinity [46]. Microthermometric analyses show that the salinity of ore-bearing fluid is about <20.89 wt. % NaCl, with the highest frequency between 0 and 5 wt. % NaCl (Figure 13b; Supplementary Table S5 and S6).

The fluid inclusions are mainly of two types (L, L-V) represented by H_2O-NaCl-vapor systems, and they range in size between <11 and 37 μm. The Type L inclusions contain a higher liquid phase, with a vapor bubble that occupies ≤10%, and they dominate (≥ 85%) in all the quartz vein samples. Type L-V inclusions are less common (vapor bubble = 10 to 15%). In addition, a rare Type V inclusion contains up to 35% vapor phase. In the Banke complex and Ririwai lode, wolframite-bearing quartz veins which cut the basement were found to have a similar three-phase inclusion [41].

Generally, the inclusions have similar cryometric parameters, as nearly all contained low to moderate saline, and low density, which showed identical ranges of homogenization temperatures (Figure 13; Supplementary Table S6). Measurements on 66 primary fluid inclusions from cassiterite- and sulfide-bearing quartz veins from the Gindi Akwati deposit yield homogenization temperatures (Th) between 143.0 and 377.2 °C and a range of freezing-point depression (Tm_{ice}) of −17.9 to 0 °C (0 to 20.89 wt. % NaCl salinity) (Supplementary Table S5 and S6). In general, inclusions from cassiterite-bearing quartz veins tend to have slightly higher homogenization temperatures for a given salinity (mean = 272.6 °C) than those from sulfide-bearing quartz veins (mean = 257.6 °C). Locally, two inclusions from cassiterite-bearing quartz veins particularly have distinctly higher homogenization temperatures (349.4 and 377.2 °C) (Figure 13c,d) than any other inclusions. Although less pronounced, a distinct salinity gap suggests that fluid mixing may be an important process in evolution [47].

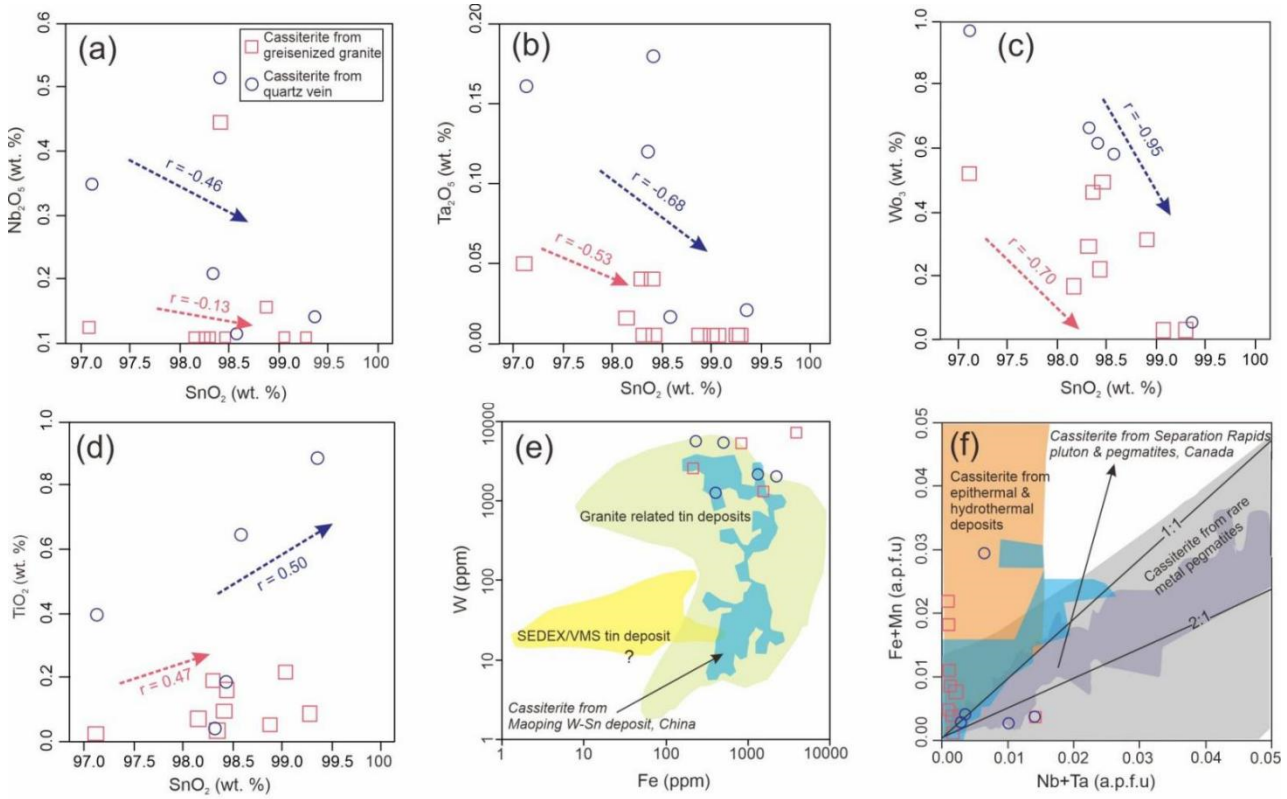

Figure 11. Binary plot of major and trace elements in cassiterite samples from the Gindi Akwati deposit. (**a**) SnO_2 vs. Nb_2O_5; (**b**) SnO_2 vs. Ta_2O_5; (**c**) SnO_2 vs. WO_3; (**d**) SnO_2 vs. TiO_2; (**e**) Fe vs. W (modified after [48]); (f) Nb + Ta (a.p.f.u) vs. Fe + Mn (a.p.f.u) (modified after [49]). Red and blue dashed arrows represent trend of correlation of cassiterite from greisenized granites and quartz veins, respectively. The r values in Figure 11a–d show the correlation coefficient.

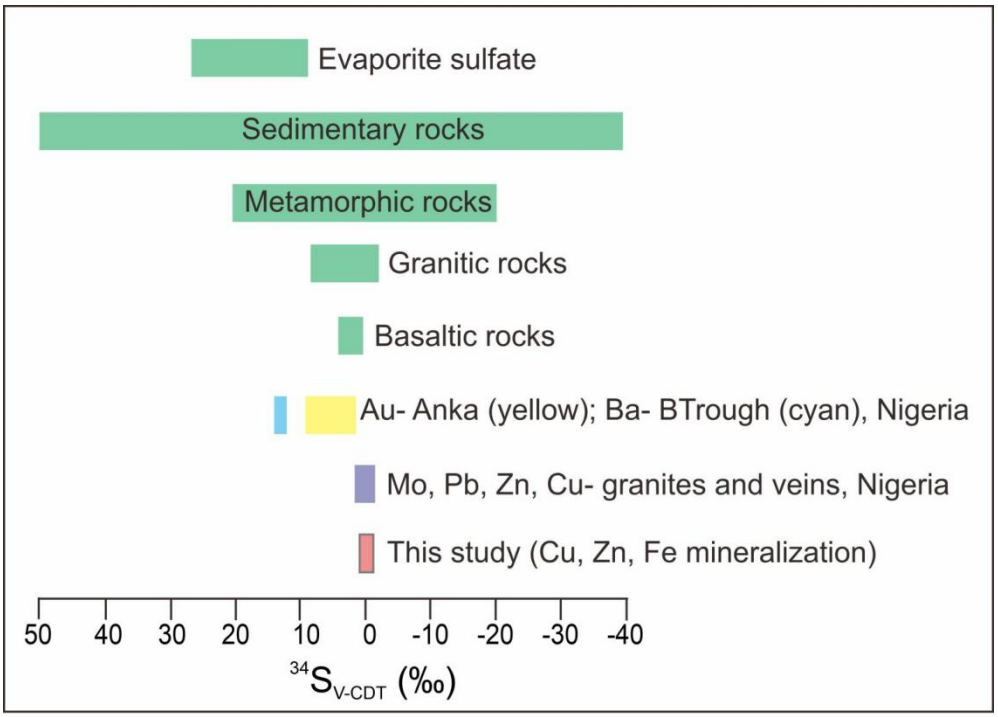

Figure 12. Sulfur isotopic compositions of the sulfides in the Gindi Akwati deposit, compared with some sulfur reservoirs (modified after [50]). The sulfur isotopic data of reservoirs in Nigeria are from previous studies in the text.

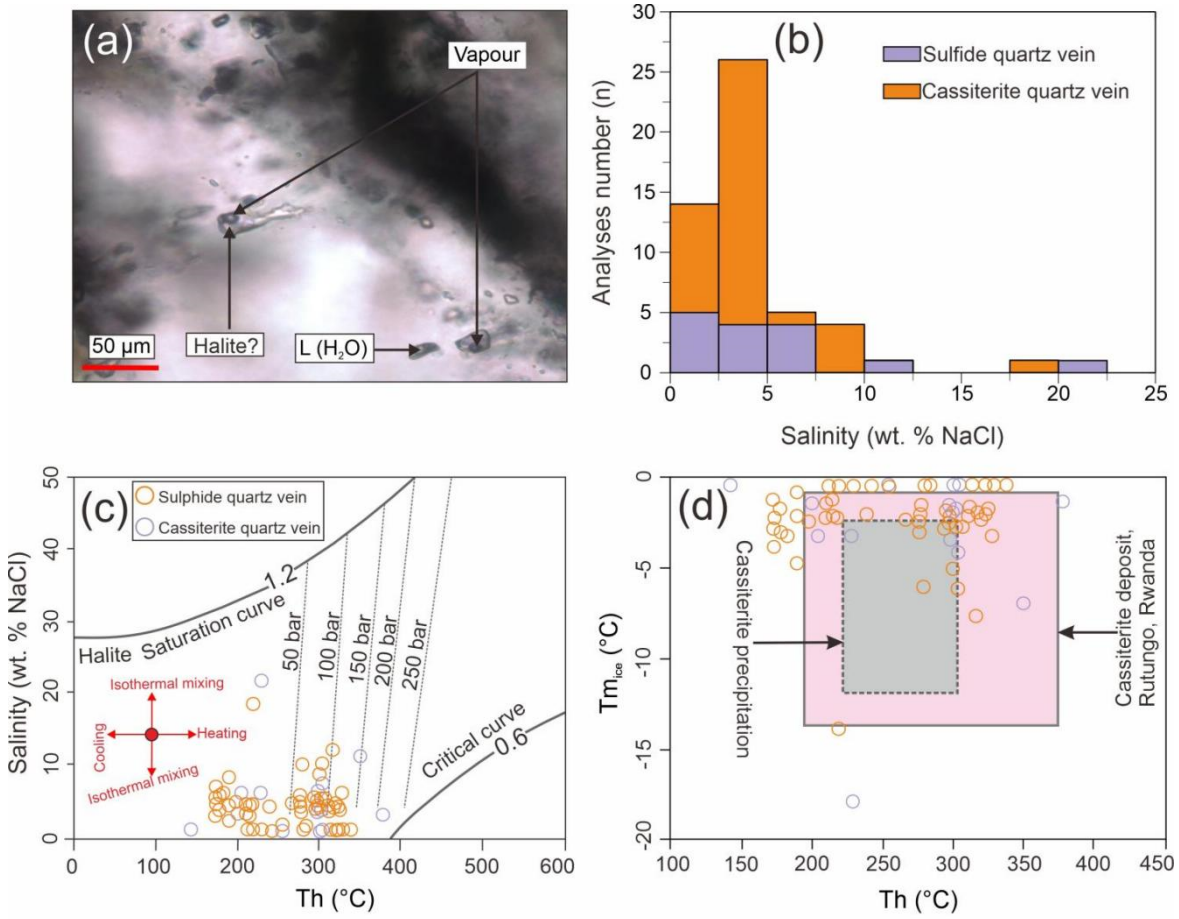

Figure 13. Microphotograph and diagram showing the relationship between salinity, homogenization temperature (Th), and final ice melting temperature (Tm_{ice}) of the fluid inclusions in cassiterite-

and sulfide-bearing quartz vein from the Gindi Akwati deposit. (**a**) Microphotograph showing the primary fluid inclusions; (**b**) Histogram of salinity (wt. % NaCl Equivalent) of sixty-six fluid inclusions; (**c**) Diagram of Salinities vs. Th (°C) with dashed lines for estimates of the vapor pressure of NaCl solution (modified from [51]). The critical-point (0.6) and halite-saturation curves (1.2) show the densities (g/cm^3) of the fluid inclusions (after [52]); (**d**) Th vs. Tm_{ice} plot of aqueous salinity inclusions from the present study, compared with the data of the ambient fluids related to the vein-type Cassiterite deposits of the Rutungo area, Rwanda [53]. It is interpreted that the cassiterite precipitation (minimum formation) occurred from the fluid under these Th and Tm_{ice} values in the field of dashed square [53]. Abbreviation: L(H_2O) = Liquid H_2O, Th = Homogenization temperature, Tm_{ice} = Final ice melting temperature.

6. Discussion

6.1. Genetic Links

The range of metal suites associated with granitic rocks depends on compositional parameters, degree of magma evolution, and oxidation states [54]. The distal Precambrian Older Granites (host rock) are barren; no ore mineral was seen except a few 0.1 to 1 mm sized grains of "magmatic" pyrite (Py1 in Figures 4b and 10). Cassiterite mineralization is commonly associated with albitization in the Jurassic biotite granites [4]. Primary mineralization of Sn, Nb, and Ta in the Nigerian Younger Granite province is contemporaneous with magmatic activity [3,37]. According to Pastor and Turaki [4], the sequences of mineralization in Nigerian Younger Granites include: (1) early cassiterite dissemination, (2) greisen formation with trioctahedral mica, minor sulfides, topaz, fluorite, and cassiterite, (3) fissure-filling veins mainly containing sulfides crosscuts greisens, and (4) veinlets and stringers containing cassiterite, wolframite, and minor sulfides. The greisenized "Older Granites" with lode-bearing and barren veins are suggested to apply to the second and third stages. They mostly formed in joints and fractures along the rims of NS-trending subvolcanic granite porphyry intrusions (Figure 2b).

Field relations, geochemistry, and mineral paragenesis all supported the coupling of hydrothermal greisens and vein mineralization to fluids originating from late-stage biotite granite consolidation. The paragenetic sequence in Figure 10 shows that greisen-hosted cassiterite is associated with local alteration of feldspars (sericitization) and formation of lepidolite (muscovitation) [55]. The mineral associations observed from optical microscopy are largely in agreement with geochemical data to confirm local alkali metasomatism and other alteration patterns [3]. For example, accessory ilmenite with a mass gain of MnO in the altered granites may define divalent manganese stability in Mg-rich ilmenite. At the same time, accessory topaz may account for the mass/volume increase in Al_2O_3, and dispersed fluorite may be due to the remobilization of CaO in greisens environments [22].

The biotite granites are highly differentiated (Figure 7e), medium to coarse-grained granites with topaz, fluorite, and ilmenite as accessory minerals which appear to be congenial for cassiterite mineralization [24]. The enrichment and depletion of some elements in the greisenized "Older Granite" largely mimicked the pattern in the Younger Granites (Figure 8). The most notable feature is the general REE behavior, in which the REE are nearly two times higher than in the host rock and about an order of magnitude lower than in the anorogenic biotite granite (Supplementary Table S2). Metasomatic greisenization of the marginal parts of Older Granite resulted from interaction with fluids that escaped from the roof zone of biotite granite during deuteric albitization. The parallelism of chondrite-normalized REE in greisenized "Older Granite" and biotite granite (Figure 8b) indicates a genetic link that allows interpretation of REE transport and fractionation in this hydrothermal system (e.g., [56]).

6.2. Mineral and Whole-Rock Chemistry Signature of the Granites

The geochemical composition has been interpreted as a function of different differentiation degrees [1]. The low values of LOI (average = 1.23 wt. %) coupled with low alteration index (≤66%) and very low Rb/Ba, Rb/Sr ratio in the greisenized granite suggests they are weakly altered (incipient greisen). Artisans' active mining has removed massive greisen, and the paucity of data from cores of massive greisenized granite obtained by Abaa [10] could not aid interpretations. Hence, we focused on the geochemical variations in the Younger Granites that constitute the source of mineralizing fluid.

The tin-bearing biotite granites in the Gindi Akwati region with high Rb and consequently low K/Rb ratio (< 200) are strongly differentiated [25,57] (Figure 7e). They are typically enriched in lithophile elements such as Rb, Cs, Nb, Ta, U, Th, Ga, and Y and depleted in Sr, Ba, Ti, Zr, and Eu. Trace element systematics of tin-bearing minerals in Nigeria Younger granites typically have high Rb content and low Sr, Ba content [58–60]. The Rb and Sn contents of biotite granites in the Gindi Akwati region have a strong positive correlation (r = 0.85). This trend is typical for other famous tin-bearing granites globally, whereby the enrichment of lithophile elements and depletion of compatible elements accompany geochemical tin speciation of tin-bearing granites [1,55].

The biotite granites with higher enrichment of Sn (average = 117 ppm) have high ratios of Rb/Sr (17.85–36.73) and Rb/Ba = (6.78–14.27) and lie within the field of tin mineralized granites in ternary Ba-Rb-Cs plot, which distinctly discriminates Sn mineralized granitic rocks from barren ones [61] (Figure 14a). The Older Granite with a relatively high Nb/Ta ratio (>5) and low Sn contents (average = 6.17 ppm) below the minimum concentration for a typical tin mineralized granite (< 15 ppm, [54]) is barren (Figure 14f). Still, the contents in weakly greisenized parts are enhanced (up to 40 ppm). According to Ballouard et al. [34], the Nb/Ta value ~5 identifies magmatic–hydrothermal transitions in peraluminous systems. The decrease in Nb/Ta ratio in the biotite granites and corresponding Sn enrichment shows a magmatic-hydrothermal transition that probably triggered the formation of ore-bearing veins in the greisenized granites of the Gindi Akwati region (e.g., [34]). Much higher values of Sn (range = 110–1330 ppm, average = 430 ppm) are reported from massive "greisens" drill cores at different depths around the Gindi Akwati region [10].

According to Lehmann [1], titanium is compatible in felsic igneous systems and relatively immobile during hydrothermal overprint, whereas tin is incompatible in the igneous systems but mobile during hydrothermal processes. During magmatic fractionation and post-magmatic alteration, the trend of the Sn-Ti plot (Figure 14b) reflects enrichment of incompatible tin and systematic depletion of titanium [62]. Hence, tin sequestrates early crystallizing Ti-bearing phases (Figure 14b). Although Ta is largely immobile during hydrothermal overprints, it is incompatible with felsic igneous processes. Thus, the enrichment of Ta is accompanied by the depletion of Ti during magmatic fractionation processes (Figure 14c), giving the best record of the igneous situation [1]. In addition, the behaviors of Zr and Ti during igneous processes and geochemical perturbation from hydrothermal fluids in highly evolved peraluminous systems are similar. The direct relations between Zr contents with trace levels of Ti that occurred in the Younger Granites of the Gindi Akwati region are consistent with those reported from other famous tin-bearing granite globally [1] (Figure 14d).

6.2.1. Fractionation Pattern of REE in the Granites

The relative enrichment of REE in the greisenized granite may indicate that the conditions during Younger Granite intrusion (biotite granite for our purposes) favored extensive REE portioning into fluids that were separated and transported into host rock fractures. These fluids contain ligands capable of complexing and transporting REE, such as fluoride, as evidenced by the presence of fluorite and topaz in the greisen. Bulk biotite

granites in Nigerian Younger Granites are known to be fluorine rich [63]. There is abundant REE incorporation into accessory fluorite, topaz, which is a significant trap at the magmatic stage; consistent with previous observations, fluorite can incorporate significant quantities of REE from a melt [56]. Thus, the occurrence of fluorite in biotite granite and greisenized granite could explain the overall pattern of REE decreasing concentration in the sequence biotite granite > greisenized granite > granite porphyry > Older Granite. The variation trend suggests that mineral-specific REE partitioning at the hydrothermal temperatures that prevailed during greisen formation was a major determinant of REE fractionation patterns within individual minerals (e.g., [56]).

6.2.2. Physicochemical Evolution of the Magmatic-Hydrothermal System

The redox state of granitic rocks is the primary control for types of metallic mineral concentration in a given ore deposit [62,64]. Although the $f(O_2)$ (oxygen fugacity) of granitoid can be slightly modified at shallow levels during solidification, the original characteristics are retained even through post-magmatic processes. Thus, the two granitoid series have an important bearing on both petrogenesis and metallogenesis [1,62]. Tin solubility in subaluminous or weakly peraluminous [A/NK= 1.02–1.22] water-saturated haplogranitic melts at 850 °C and $f(O_2)$ around 2 $\log_{10}$ units or more above the FMQ (fayalite–magnetite–quartz) buffer has been determined experimentally to be ~400 ppm SnO_2. Because the solidus temperature of highly evolved fluorine-rich granite is around 600 °C or lower [65], the saturation concentration of cassiterite in such granites may be well below 400 ppm Sn under low $f(O_2)$ conditions. Changes in pressure conditions do not exert any significant influence on tin concentration in granitic melts. However, the solvent capacity of the granitoid melts is increased by decreasing $f(O_2)$ and increasing temperature [24].

The zircon saturation temperatures estimated in the biotite granite range from 739 to 804 °C, with an average temperature of 754 °C after the calculation method from Watson and Harrison [66], and those temperatures obtained after another thermometer by Boehnke et al. [67] range from 736 to 785 °C, with an average temperature of 747 °C (Supplementary Table S2). In addition, the ferric/ferrous bulk ratio (wt. %) of the granitic rocks (< 0.2; low $f(O_2)$) is far less than the separation line ($Fe_3O_2/FeO = 0.5$ and $SiO_2 = 70$ wt. %) between magnetite- and ilmenite-series granitoid [68] (Figure 14e). Differing with the Peruvian plutonic rocks from the authors cited in Ishihara et al. [68], tin and tungsten mineralization are related to the ilmenite-series granites and the Younger Granite in Gindi Akwati deposit plot in the ilmenite-series field under the broken line. Moreover, their plot in the ilmenite-series of FeO + MnO − Fe_2O_3 + TiO – MgO ternary diagram indicates depleted MgO and the general reduced nature of the Jurassic granites [69] (Figure 14f). This suggests $f(O_2)$ of bulk rock is a log unit or more above the FMQ buffer around the NNO buffer boundary (e.g., [64]). Globally, tin and tungsten mineral deposits are associated with ilmenite-series granitoid due to their reduced form [1,62]. The magmatic tin enrichment trend with distribution coefficient D_{Sn} (crystals/melt) < 1 at $f(O_2)$ below the NNO buffer is realized in ilmenite-series granitic rocks (S-, I-, A-type). This is also a requirement for efficient hydrothermal depletion of magmatically tin-enriched rock volumes [1].

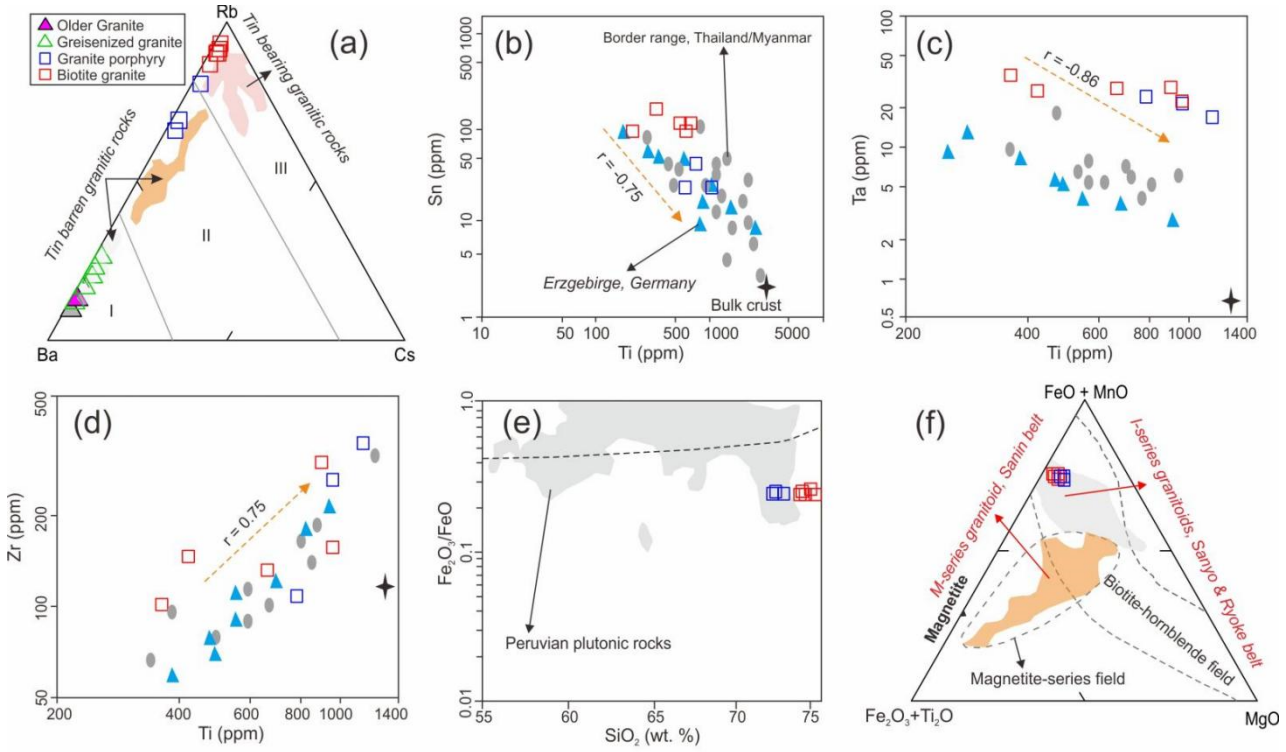

Figure 14. Magmatic discrimination plots of Older Granite, greisenized granite, and Younger Granite (including granite porphyry and biotite granite) from the Gindi Akwati deposit. (**a**) Rb–Ba–Cs diagram for granitic rocks, three areas distinguished: I = Sn ≤ 15 ppm, Rb/Ba < 0.48, Rb/Sr < 1.3; II = Sn > 15 ppm, 0.48 < Rb/Ba < 5, 1.3 < Rb/Sr < 15; III = Sn > 29 ppm, Rb/Ba > 5, Rb/Sr > 15 (after [61]); (**b**–**d**) Diagram of Sn vs. Ti, Ti vs. Ta and Ti vs. Zr for the Younger Granite in Gindi Akwati deposit and other granites related to tin mineralization from Thailand/Myanmar and Germany showing Sn sequestration into early crystallizing Ti-bearing phases (after [6,62]); (**e**) Diagram of Fe_2O_3/FeO vs. SiO_2 (wt. %) for the Younger Granites. The broken line is a separation line between magnetite-series and ilmenite-series (after [68]); (**f**) Diagram of $Fe_2O_3 + TiO_2 – MgO – FeO + MnO$ for the Younger Granite in Gindi Akwati deposit, showing that the samples lie in the ilmenite-series field (after [69]). For Figure 14e and f, the FeO and Fe_2O_3 from total iron contents were calculated by using the excel spreadsheet in the article of Yang et al. [70].

6.2.3. Metal Partitioning

At the intrusion and deposit scale, the partitioning of metals in granitic rocks may reflect these elements contrasting behavior during late-stage or post-magmatic processes (e.g., [71]). An indication from petrography, with the lack of tourmaline and accessory fluorite and topaz in the granites, rules out boron and confirms fluorine. Fluoride is important in the transport of some metals/elements in hydrothermal ore solutions, including titanium, tin, REE, zirconium, and uranium [72]. The importance of tin (II) fluoride complexes, such as $SnF(OH)_2^-$ and SnFCl, in hydrothermal fluoride solutions at 500 °C and 1 kbar have been demonstrated, but more experimentally based thermodynamic data are needed to fully comprehend the mechanism [72].

Chlorine is the most common halogen responsible for complexing ligands that sequestrate metals and transport them in hydrothermal solutions [1,71,73]. However, the precipitation of tin as a cassiterite involves oxidation [1]. As a result, the efficiency of complexing and transporting ore elements (Cu, Sn, Au, Pb, Zn, Ag) by Cl is dependent on Cl partitioning between melts and aqueous fluid phase, hydroxide, and alkali hydroxide species, and it is reduced to oxidized S complexes [54,73].

A quantitative measure of partition coefficients for metals (Pb, Cu, Zn, Fe, and Sn) from co-existing fluid/melt inclusions in peralkaline to peraluminous granitic systems at $f(O_2)$ = NNO − 1.7 to NNO + 4.5 and 1 to 14 mol/kg chlorinity has been demonstrated in

an experimental study [74]. The partition coefficient of Fe, Zn, and Cu is known to increase with increasing chlorinity (other ligands may play a role for Cu), which suggests increasing chlorinity favors the dissolution of metals. Partition coefficients for Sn are highly variable, but they are likely to increase with increasing fluid chlorinity and decrease with decreasing $f(O_2)$ or melt peraluminousity [54,74].

The valence states of tin in reduced and oxidized granite melts are divalent (Sn^{2+}) and tetravalent (Sn^{4+}) forms, respectively [75]. Under high $f(O_2)$ conditions (Fe^{3+}/Fe^{2+} ratio >0.5), tin in the tetravalent state may be incorporated into accessory minerals, such as magnetite, sphene, and ilmenite during the early stages of crystallization, resulting in a relatively low tin concentration in later stages [1,6,54]. The contrast probably prevailed around the Gindi Akwati region (low $f(O_2)$ magmas; Fe^{3+}/Fe^{2+} ratio < 0.5). Tin is predominantly bivalent, which prevents it from entering rock-forming minerals and favors accumulation in residual liquids.

On the other hand, the formation of the sulfide ores depends on T and $f(O_2)$. The dominant sulfur species in the hydrothermal fluid is a function of redox condition (H_2S in reduced condition or SO_2 in the oxidized state). Sulfur is more soluble in oxidized melts than in reduced melts for any given FeO content, and related precipitation elements such as Pb, Zn, Cu, Mo, Co, As, Bi, and Au will be partitioned into early sulfides rather than concentrated in late-stage melts and a later exsolving aqueous phase [54]. The $f(O_2)$ of granitic rocks in the present studies are below the NNO buffer, which preliminarily suggests S is present as a sulfide. The bulk partition coefficient of S between the aqueous fluid and melt at low $f(O_2)$ and high pressure will cause early precipitation of sulfides, consequently preventing the formation of significant deposits [1,54]. The constraints on ore-forming conditions from fluid inclusion and isotopic studies are discussed below.

The co-existence of cassiterite, chalcopyrite, and Li-rich mica (lepidolite) in the "weakly" greisenized granites (Figure 6e) indicates that some volatility in the system, at least temporarily, sequestered Li, Sn, and Cu from the melt (e.g., [76]). We postulate that ore metal deposition involves reactions from remobilized portions of the Older Granite by volatile-rich fluids (Cl-rich for our purpose). The progressive activity of Na^+, K^+, and H^+ ions in the cooling greisenized parts complexed to form metal chloride solutes, which were then converted into oxide or sulfide minerals [73].

6.3. Source of Fluid and Ore Metals in the Gindi Akwati Region

An influx of volatile-rich hydrothermal fluid that escaped from roof zones of biotite granite transported ores through shears at the margins of the host granite [10,77]. Therefore, we constrained the ore-forming conditions from sulfur isotope and fluid inclusion studies. This includes $f(O_2)$, density, fluid salinity, trapping temperature, and pressure. In addition, the sources of cassiterite and sulfide ores are discussed in detail below.

6.3.1. Ore-Forming Conditions

Higher oxidation states of sulfur are more enriched in heavier isotopes than lower oxidation states, so ^{34}S enrichment follows the general trend $SO_4^{2-} > SO_3^{2-} > S_x^0 > S^{2-}$ [78]. Oxidation-reduction reactions and other geochemical processes fractionate sulfur away from bulk-Earth values (reference reservoirs) in geological systems [79]. The notable absence of sulfate minerals or magnetite (heavier isotopes) suggests the sulfur is not in a higher oxidation state. Sulfide (H_2S, HS^- and S^{2-}) constitutes the reductive end of the geochemical sulfur cycle. In the preceding statements, we indicated that the fractionation of sulfur varies depending on environmental chemical conditions of redox state. The heavier isotope (^{34}S) is preferentially bound in sulfate relative to that in co-existing sulfide. Consequently, sulfur dioxide (SO_2) should be the most important sulfur species in high fO_2 magmatic hydrothermal systems, whereas H_2S, HS^-, and S^{2-} are the dominant reduced sulfur species [79]. Hence, the $\delta^{34}S$ in the hydrothermal system at the ore-forming stage in the mapped strip was dominated by H_2S, HS^-, and S^2, where ores were formed under low fO_2 and low pH (acidic) conditions.

The liquid-rich primary inclusions (liquid-vapor type) in the quartz veins are trapped by sealing growth irregularities in the host crystal [51]. The thermal and chemical gradients within the ore deposits may account for the variations in homogenization temperature (Th) and salinity in the inclusions [51]. The dominance of primary inclusions with high proportions of liquid phase with narrow ranges of measured homogenization temperatures suggests the trapping of the homogenous fluid phase (Figure 13d), equivalent to the minimum possible formation temperature (e.g., [51]). The trapping pressures during the ore-forming stage are estimated to range from <50 bar to 200 bar and are mostly concentrated in the range from <50 bar to 100 bar (Figure 13c), which would correspond to depths of ~0.3–1.2 km, assuming cold hydrostatic conditions [80]. The variations indicate a sudden pressure drop and the constrained pressure release generated by the ores (e.g., [41]). Furthermore, it seems clear that ore deposits cannot be generated without separating a vapor phase [51].

The salinity of the inclusions from cassiterite- and sulfide-bearing quartz veins was largely overlapped. Still, variations in homogenization temperature suggest the ore-forming process may have taken place in two stages, or it may have acted in a continuous progression [81]. The mineralized veins lie within greisenized granite that is commonly associated with the alteration. Extensive alteration reflects disequilibrium and the intensity of greisenization attained during fluid–rock reactions. As a result, the chemical equilibrium between the mineralizing fluids and the quartz vein wall rocks implies that the mineralizing fluids are penecontemporaneous with the magmatic fluid that caused greisenization. These probably control the dominance of liquid-rich fluid inclusions (e.g., [82]).

Although the measured homogenization temperature (Th) values of inclusions from cassiterite- and sulfide-bearing quartz veins overlap (143.0–377.2 °C and 172.4–337.7 °C, respectively), two points have very low ice melting temperature (Tm) and high salinity (up to −17.9°C) but are still below the eutectic temperature of aqueous fluid inclusions (-21.2 °C; ice + $NaCl{\cdot}2H_2O$) in the salt-water system [83]. Nearly all the inclusions from sulfide-bearing quartz veins have low salinity, except for one (up to 17.70 wt. % NaCl). In addition, one inclusion from cassiterite-bearing quartz veins hosts more saline fluids (up to 20.89 wt. % NaCl). A relative inverse correlation between ice melting temperature (Tm) and homogenization temperature (Th) could indicate a dilution of a hot, saline magmatic fluid (Th >300 °C) with low salinity meteoric water (e.g., [84]) (Figure 13d).

The entrapped fluids are primary two-phase (liquid-vapor) with a salinity range between 20.89 to 0 wt. % NaCl (average = 4.08 wt. % NaCl). This suggests a decrease in the salinity of hydrothermal fluids during the evolution. The subtle variation in salinity, combined with low homogenization temperature (highest frequency = 143 to 300 °C), is very characteristic of post-magmatic hydrothermal mineralization at low temperature [85]. In addition, the few relatively high homogenization temperature datasets suggest that a compositionally heterogeneous fluid was formed by fluid boiling (Figure 13c) and CO_2 immiscibility (from a few high-pressure estimates of the pressure of 150 to >200 bar) at temperatures above 300 °C (e.g., [84]). The stage at which the precipitation of major ores (Sn, Cu, Zn, Fe) occurred is mainly characterized by trapping pressure <200 bar and discernible mineral assemblages in the greisen. This suggests the mineralization veins started with hot (homogenization temperature ≥300 °C), low to moderate salinity (average = 4.08 wt. % NaCl), low density (≤0.6 g/cm^3) fluids, and ≥ 200 bar trapping pressure (Figure 13c).

6.3.2. Cassiterite Source and Growth Environment

Cassiterite of various genetic types can have varying chemical compositions. Minor elements Nb, Ta, Fe, and Mn are abundant in magmatic cassiterite, which is related to highly fractionated Li–F granite and pegmatite. Hydrothermal cassiterite, on the other hand, typically has low Nb and Ta contents (e.g., [49]). Except for when W is high, all the minor elements are moderate in the quartz vein and low in the greisenized granite. However, the greisenized granite cassiterite has high Fe content. The systematic variation in W

and Fe contents in cassiterite from both greisen and quartz veins in the Gindi Akwati region is similar to that found in granite-related Sn deposits around the world (e.g., [86]) (Figure 11e).

The cassiterite from quartz vein and a few from greisen fall along with a linear array, with Fe + Mn and Nb + Ta predominantly varying in the ratio of 2:1 corresponding to the coupled substitution: $3Sn^{4+} = 2(Nb, Ta)^{5+} + (Fe, Mn)^{2+}$ (e.g., [49,86]) (Figure 11f). In addition, a few cassiterites from greisen have compositions approaching the 1:1 substitution line, suggesting the presence of a $Fe^{3+}(Nb, Ta)O_4$ component in some of the cassiterite, consistent with the substitution: $2Sn^{4+} = Fe^{3+} + Ta^{5+}$ (e.g., [49]) (Figure 11f). Tetravalent elements readily substitute directly for Sn^{4+} without any charge balance considerations. On the other hand, Nb and Ta occur as 5^+ ions, whereas Fe can be divalent or trivalent. Therefore, some of the greisenized granite cassiterite with very low Mn, Nb, and Ta, but significant Fe, needs an additional mechanism to incorporate Fe cations. We propose the coupled substitution: $Fe^{3+} + OH^- = Sn^{4+} + O^{2-}$ (e.g., [86]).

Although most of the greisenized granite and quartz vein cassiterites are hydrothermal cassiterite, others exhibit magmatic signatures with a variable mechanism of substitution. High Nb, Ta, and low Ti indicate cassiterite crystallization in a high-temperature environment [87]. The low (in greisen) to high (in quartz veins) Ti contents, and relatively low Nb and Ta contents in all cassiterite, suggest they crystallized at moderate to low temperature. Therefore, we inferred that cassiterite growth was governed by hot, magmatically derived fluids (possibly without contribution from cooler exogranitic fluids and/or meteoric water) contemporaneous with the greisenization process.

6.3.3. Sulfur Sources in the Sulfides

In geochemical processes, stable isotopes of sulfur (S) are important tracers for ore-forming material sources [79]. The main sources of sulfur are: (1) inorganic reduction in seawater sulfate, (2) sulfur leaching from igneous footwall rocks, (3) mantle magmatic fluids, and (4) sulfur from microbial activity in reduced sediments [50].

Generally, the minor variability of the measured data suggests a uniform sulfur source. At the same time, the near-zero $\delta^{34}S$ values are typically considered to indicate an igneous origin, either directly by magma devolatilization or by leaching from local intrusions (e.g., [88]). According to the established order of sulfide formation, the $\delta^{34}S_{V\text{-}CDT}$ values of these grains decrease systematically from sphalerite to pyrite and chalcopyrite (0.87 to −1.30‰) (Supplementary Table S4), probably implying that the main mineralization stage developed in a stable and uniform hydrothermal environment [79]. The relationship $\delta^{34}S_{H2S} \approx \delta^{34}S_{fluid}$ holds in the equilibrium state and can be used to trace the sulfur source [89]. The calculated $\delta^{34}S_{H2S}$ (−1.93‰ to 0.51‰, average = −0.49‰) are similar to those of the famous tungsten deposit associated with granite intrusions in Xihuashan (−0.83‰) in the Nanling region [90], Dengfuxian (−0.63‰) in the Hunan province [91], and Yaoling (−0.07‰) in South China [89] that are interpreted to be of magmatic origin. The narrow ranges of $\delta^{34}S_{V\text{-}CDT}$ values for the ores, as well as the close temporal-spatial association of the ore bodies and the granite, not only indicate that the Gindi Akwati region's sulfur sources are magmatic but also that the source of S was homogenous (e.g., [89]) (Figure 12). As a result, the sulfides are formed from a single fluid that contains both metal and sulfur and precipitates, as a result of a change in physical and chemical conditions (e.g., [92]).

6.4. Genetic Model

The Jurassic granite porphyry pluton in the mapped strip is a forceful (active) intrusion that explores the east-west oriented extensional component. The intrusion wall and roof created a local shear-sense (few to tens of cm) within the margins of the basement Older Granites, which defines the NS trend of its long axis (Figures 2b and 15). The porosity and permeability in sheared Older Granite enhanced the movement of ore-bearing fluids that escaped during the late-stage consolidation of the biotite granite. The rheology

of the Older Granite dictates the mechanism of fluid–rock interaction that induced greisenization (e.g., [93]). The extent of fluid–rock reactions controlled the recrystallization of new minerals at the incipient and massive greisen zones (Figure 15).

The contact relations and physical characteristics suggest that both the cassiterite–sulfide mineralization in the greisen and quartz veins are not only spatially related but also coeval with the greisenization of portions of the Older granite in the vicinity to the minor shear(s) (Figure 15). This explains why the greisenized parts (containing disseminated and lode vein mineralization) are strictly restricted to areas in the vicinity of the shears (e.g., [94]). Some forms of magmatic tin enrichment via fractional crystallization in biotite granite and subsequent hydrothermal redistribution are favored by a redox state at or below the NNO buffer (e.g., [1]). The low P-T variation from fluid inclusion studies also supports that the mineralized quartz veins are from a late magmatic fluid stage contemporaneous with greisenization [95].

It is well known that some oxides co-exist with sulfides under certain physicochemical conditions and therefore crystallize at the same time [96]. For example, cassiterite is stable with chalcopyrite, sphalerite, and galena in certain environments. However, the sulfides become unstable at redox potential (Eh) >0.2 V, whereas cassiterite remains stable at Eh >1 V [97]. The difference in the abundance of ores with depth can be explained by assuming the sulfides had an isomorphic admixture of tin, to which effects of high redox potential (Eh) at apical parts made the sulfides unstable and decomposed, liberating SnO_2 in the reaction of Sn with oxygen (e.g., [97,98]) (Figure 15).

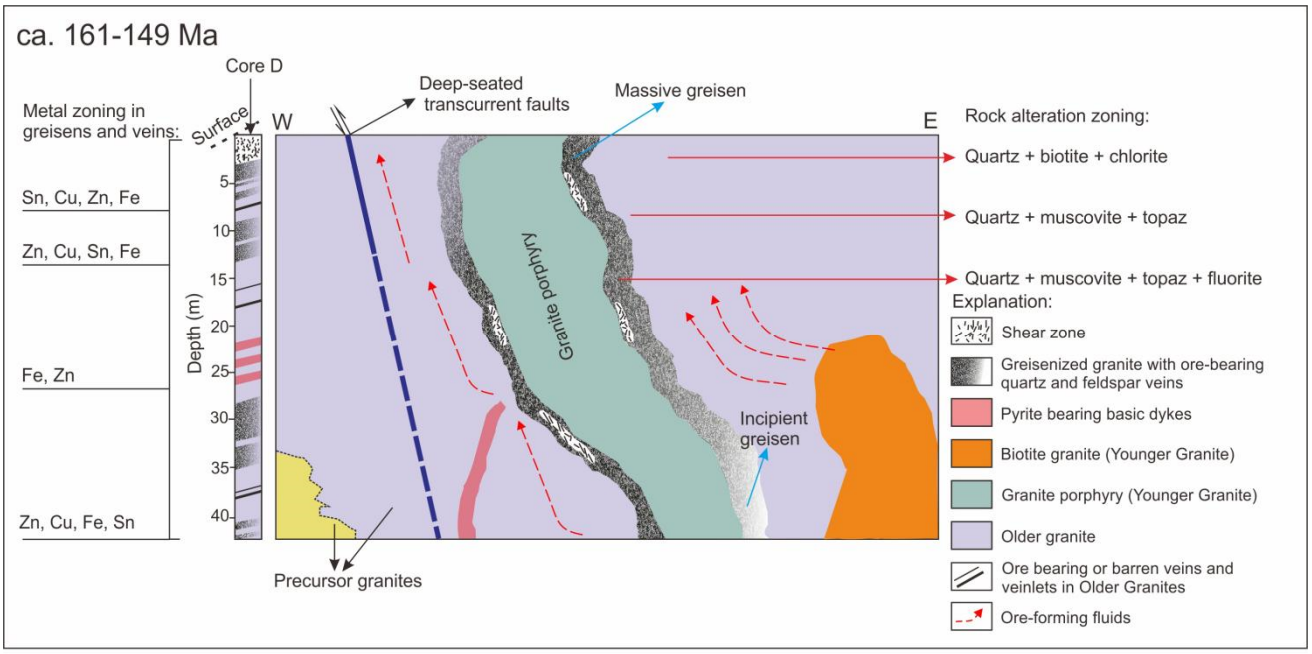

Figure 15. Simplified magmatic-metallogenic model (not to scale) within ca. 161 to 149 Ma after over 400 Ma hiatus, pressure released from reactivated transcurrent fault triggered partial melting, followed by forceful emplacement of the Jurassic granite porphyry, which sheared the Older Granites (modified after [59,99]). Mineralized fluids that escaped from the roof zone of biotite granite intrusion moved through the shears, altered, and mineralized the precursor rocks around the vicinity of the shears.

7. Conclusions

(1). The forceful intrusion of Jurassic Younger granite porphyry sheared parts of the host rock (Precambrian Older Granite) in the Gindi Akwati region. Fluids that escaped during late-stage consolidation of a later intrusion (Jurassic biotite granite) greisenized marginal parts of the Older Granite. The compositional variations in the biotite granite show they are highly evolved in low oxygen fugacity conditions that favor tin mineralization.

(2). The hydrothermal alteration that occurs with attendant mineralization is in three stages, i.e., an early one with a high-temperature stage characterized by feldspar and quartz replacements that induced greisenization; an intermediate-temperature stage, where volatile-rich fluids complexes partitioned metals, characterized by crystallization of lepidolite (Li-rich muscovite), fluorite, topaz, and apatite and accompanied by the introduction of oxide and sulfides in greisenized granites; and a depositional hydrothermal stage that formed quartz veins bearing sulfides and tin.

(3). Constraints from stable isotope and fluid inclusion systematics show the hydrothermal history of greisens and veins began with hot, low to moderate saline fluids, which had an isotopic composition very close to that of typical magmatic fluids at or below the NNO buffer. This favors late magmatic to early post-magmatic models of mineralization related to the anorogenic Jurassic biotite granite intrusion.

Supplementary Materials: The following supporting information can be downloaded at: https://www.mdpi.com/article/10.3390/min12060761/s1, Table S1: Modal compositions (wt. %) of Older Granite, greisenized granite, greisen wall-rock, granite porphyry, and biotite granite from the Gindi Akwati deposit, north-central Nigeria; Table S2: Major element (wt. %), trace element (ppm), and REE (ppm) contents of the Older Granite (including altered parts) and Younger Granite in the Gindi Akwati deposit, north-central Nigeria; Table S3: Representative compositions of cassiterite (mean of three measurements from the core to rim in quartz veins and spots in the greisenized granites) from the Gindi Akwati deposit, north-central Nigeria; Table S4: Sulfur isotopic compositions of the sulfides from quartz veins and greisenized granite from the Gindi Akwati deposit, north-central Nigeria; Table S5: Primary microthermometry results of the sixty-six fluid primary inclusions from cassiterite- and sulfide-bearing quartz veins from the Gindi Akwati deposit, north-central Nigeria. L-V = Liquid-Vapor; Table S6: Summary of microthermometry data of the sixty-six primary fluid inclusions from cassiterite- and sulfide-bearing quartz veins from the Gindi Akwati deposit, north-central Nigeria.

Author Contributions: A.K.A. and S.L. wrote the article; X.Y. made the analyzed plans in this study and J.C. did the systematic analysis; M.F. took part in the field investigation; X.Y. revised the manuscript. All authors have read and agreed to the published version of the manuscript.

Funding: This work is financially supported by the National Key Research and Development Program of China (Grant No. 2016YFC0600404) and the National Natural Science Foundation of China (Nos. 41803038, 42030801, 42011540384).

Acknowledgments: We appreciate the great help from Sidikat Lami Salau of the initiative for Advancement of Mining, Earth Science and Environmental Protection, Abuja. We also appreciate the great help from Suleiman Shehu Magaji of the Department of Geology, Ahmadu Bello University, Zaria and Paul O Ogunleye of the Centre for Energy Research and Training, Ahmadu Bello University, Zaria for providing logistical support during the sample collection.

Conflicts of Interest: The authors declare no conflict of interest.

References

1. Lehmann, B. Formation of tin ore deposits: A reassessment. *Lithos* **2020**, *402–403*, 105756. https://doi.org/10.1016/j.lithos.2020.105756.
2. René, M. Petrology, geochemistry and mineralogy of greisens associated with tin-tungsten mineralisation: Hub Stock deposit at Krásno-Horní Slavkov ore district, Czech Republic. In *Contributions to Mineralization*; Al-Juboury, A.I., Ed.; IntechOpen: London, UK, 2018; pp. 901–930. https://doi.org/10.5772/intechopen.71187.

3. Kinnaird, J. Hydrothermal alteration and mineralization of the alkaline anorogenic ring complexes of Nigeria. *J. Afr. Earth Sci. (1983)* **1985**, *3*, 229–251. https://doi.org/10.1016/0899-5362(85)90038-7.
4. Pastor, J.; Turaki, U. Primary mineralization in Nigerian ring complexes and its economic significance. *J. Afr. Earth Sci. (1983)* **1985**, *3*, 223–227. https://doi.org/10.1016/0899-5362(85)90037-5.
5. Goodenough, K.; Lusty, P.; Roberts, N.; Key, R.; Garba, A. Post-collisional Pan-African granitoids and rare metal pegmatites in western Nigeria: Age, petrogenesis, and the 'pegmatite conundrum'. *Lithos* **2014**, *200–201*, 22–34. https://doi.org/10.1016/j.lithos.2014.04.006.
6. Lehmann, B. Metallogeny of tin; magmatic differentiation versus geochemical heritage. *Econ. Geol.* **1982**, *77*, 50–59. https://doi.org/10.2113/gsecongeo.77.1.50.
7. Melcher, F.; Graupner, T.; Gäbler, H.-E.; Sitnikova, M.; Henjes-Kunst, F.; Oberthür, T.; Gerdes, A.; Dewaele, S. Tantalum–(niobium–tin) mineralisation in African pegmatites and rare metal granites: Constraints from Ta–Nb oxide mineralogy, geochemistry and U–Pb geochronology. *Ore Geol. Rev.* **2013**, *64*, 667–719. https://doi.org/10.1016/j.oregeorev.2013.09.003.
8. Benkhelil, J. The origin and evolution of the Cretaceous Benue Trough (Nigeria). *J. Afr. Earth Sci.* **1989**, *8*, 251–282. https://doi.org/10.1016/s0899-5362(89)80028-4.
9. Matheis, G. Nigerian rare-metal pegmatites and their lithological framework. *Geol. J.* **1987**, *22*, 271–291. https://doi.org/10.1002/gj.3350220620.
10. Abaa, S.I. The Geochemistry, Petrology and Mineralization at Ririwai, Gindi Akwati and Dutsen Wai in the Nigerian Younger Granite Province. Master's Thesis, Ahmadu Bello University, Zaria, Nigeria, 1976; p. 16. Available online: http://kubanni.abu.edu.ng/jspui/handle/123456789/197 (accessed on 13 June 2022).
11. Schlüter, T. Geological Atlas of Africa: With Notes on Stratigraphy, Tectonics, Economic Geology, Geohazards, Geosites and Geoscientific Education of Each Country. Springer-Verlag: Berlin, Heidelberg, 2008, pp. 1-100. https://doi.org/10.1007/978-3-540-76373-4.
12. Garba, I. Geochemical characteristics of mesothermal gold mineralisation in the Pan-African (600 ± 150 Ma) basement of Nigeria. *Appl. Earth Sci.* **2003**, *112*, 319–325. https://doi.org/10.1179/037174503225003143.
13. Llorens, T.; Moro, M.C. Oxide minerals in the granitic cupola of the Jálama Batholith, Salamanca, Spain. Part I: Accessory Sn, Nb, Ta and Ti minerals in leucogranites, aplites and pegmatites. *J. Geosci.* **2012**, *57*, 25–43. https://doi.org/10.3190/jgeosci.113.
14. Liu, Y.; Liu, H.C.; Li, X.H. Simultaneous and precise determination of 40 trace elements in rock samples using ICP-MS. *Geochimica* **1996**, *25*, 552–558. (In Chinese with English abstract)
15. Qi, H.; Lu, S.; Yang, X.; Zhao, L.; Zhou, Y.; Deng, J.; Li, J. Genesis of Cretaceous igneous rocks and its related large scale porphyry Cu-Au mineralization in Chating, the Middle-Lower Yangtze River Metallogenic Belt: The geochemical constrains. *Ore Geol. Rev.* **2020**, *127*, 103793. https://doi.org/10.1016/j.oregeorev.2020.103793.
16. Bao, Z.; Chen, L.; Zong, C.; Yuan, H.; Chen, K.; Dai, M. Development of pressed sulfide powder tablets for in situ sulfur and lead isotope measurement using LA-MC-ICP-MS. *Int. J. Mass Spectrom.* **2017**, *421*, 255–262. https://doi.org/10.1016/j.ijms.2017.07.015.
17. Chen, L.; Chen, K.; Bao, Z.; Liang, P.; Sun, T.; Yuan, H. Preparation of standards for in situ sulfur isotope measurement in sulfides using femtosecond laser ablation MC-ICP-MS. *J. Anal. At. Spectrom.* **2016**, *32*, 107–116. https://doi.org/10.1039/c6ja00270f.
18. Yuan, H.; Liu, X.; Chen, L.; Bao, Z.; Chen, K.; Zong, C.; Li, X.-C.; Qiu, J.W. Simultaneous measurement of sulfur and lead isotopes in sulfides using nanosecond laser ablation coupled with two multi-collector inductively coupled plasma mass spectrometers. *J. Southeast Asian Earth Sci.* **2017**, *154*, 386–396. https://doi.org/10.1016/j.jseaes.2017.12.040.
19. Bodnar, R. Revised equation and table for determining the freezing point depression of H2O-Nacl solutions. *Geochim. Cosmochim. Acta* **1993**, *57*, 683–684. https://doi.org/10.1016/0016-7037(93)90378-a.
20. Vry, V.H.; Wilkinson, J.J.; Seguel, J.; Millan, J. Multistage Intrusion, Brecciation, and Veining at El Teniente, Chile: Evolution of a Nested Porphyry System. *Econ. Geol.* **2010**, *105*, 119–153. https://doi.org/10.2113/gsecongeo.105.1.119.
21. Winchester, J.; Floyd, P. Geochemical discrimination of different magma series and their differentiation products using immobile elements. *Chem. Geol.* **1977**, *20*, 325–343. https://doi.org/10.1016/0009-2541(77)90057-2.
22. Lentz, D.R.; Lutes, G.; Hartee, R. Bi-Sn-Mo-W greisen mineralization associated with the True Hill granite, southwestern New Brunswick. *Atl. Geol.* **1988**, *24*, 321–380. https://doi.org/10.4138/1660.
23. Rudnick, R.L.; Gao, S. Composition of the Continental Crust. In *Treatise on Geochemistry*; Holland, H.D., Turekian, K.K., Eds.; Elsevier: Amsterdam, The Netherlands, 2003, Volume 3, pp. 1–64. https://doi.org/10.1016/B978-0-08-095975-7.00301-6.

24. Babu, T.M. Comparative Studies of Tin Fertile Granitic Rocks in Space and Time. *Resour. Geol.* **1993**, *43*, 355–363. https://doi.org/10.11456/shigenchishitsu1992.43.355.
25. El Bouseily, A.; El Sokkary, A. The relation between Rb, Ba and Sr in granitic rocks. *Chem. Geol.* **1975**, *16*, 207–219. https://doi.org/10.1016/0009-2541(75)90029-7.
26. Lehmann, B.; Ishihara, S.; Michel, H.; Miller, J.; Rapela, C.W.; Sanchez, A.; Tistl, M.; Winkelmann, L. The Bolivian tin province and regional tin distribution in the Central Andes; a reassessment. *Econ. Geol.* **1990**, *85*, 1044–1058. https://doi.org/10.2113/gsecongeo.85.5.1044.
27. Olade, M.A. Geochemical characteristics of tin-bearing and tin-barren granites, northern Nigeria. *Econ. Geol.* **1980**, *75*, 71–82. https://doi.org/10.2113/gsecongeo.75.1.71.
28. Taylor, S.R.; McLennan, S. The geochemical evolution of the continental crust. *Rev. Geophys.* **1995**, *33*, 241–265. https://doi.org/10.1029/95rg00262.
29. Baumgartner, L.P.; Olsen, S.N. A least-squares approach to mass transport calculations using the isocon method. *Econ. Geol.* **1995**, *90*, 1261–1270. https://doi.org/10.2113/gsecongeo.90.5.1261.
30. Štemprok, M.; Pivec, E.; Langrová, A. The petrogenesis of a wolframite-bearing greisen in the Vykmanov granite stock, Western Krušné hory pluton (Czech Republic). B. Geosci. **2005**, *80*, 163–184.
31. Launay, G.; Sizaret, S.; Guillou-Frottier, L.; Fauguerolles, C.; Champallier, R.; Gloaguen, E. Dynamic permeability related to greisenization reactions in Sn-W ore deposits: Quantitative petrophysical and experi-mental evidence. *Geofluids* **2019**, *2019*, 1-23. https://doi.org/10.1155/2019/5976545.
32. Peccerillo, A.; Taylor, S.R. Geochemistry of eocene calc-alkaline volcanic rocks from the Kastamonu area, Northern Turkey. *Contrib. Miner. Petrol.* **1976**, *58*, 63–81. https://doi.org/10.1007/bf00384745.
33. Frost, B.R.; Barnes, C.G.; Collins, W.J.; Arculus, R.J.; Ellis, D.J.; Frost, C.D. A Geochemical Classification for Granitic Rocks. *J. Pet.* **2001**, *42*, 2033–2048. https://doi.org/10.1093/petrology/42.11.2033.
34. Ballouard, C.; Poujol, M.; Boulvais, P.; Branquet, Y.; Tartèse, R.; Vigneresse, J.L. Nb-Ta fractionation in peraluminous granites: A marker of the magmatic-hydrothermal transition. *Geology* **2016**, *44*, 231–234.
35. Anders, E.; Grevesse, N. Abundances of the elements: Meteoritic and solar. *Geochim. Cosmochim. Acta* **1989**, *53*, 197–214. https://doi.org/10.1016/0016-7037(89)90286-x.
36. Grant, J.A. Isocon analysis: A brief review of the method and applications. *Phys. Chem. Earth, Parts A/B/C* **2005**, *30*, 997–1004. https://doi.org/10.1016/j.pce.2004.11.003.
37. Kinnaird, J.; Bowden, P. African anorogenic alkaline magmatism and mineralization-a discussion with reference to the Niger-Nigerian province. Geol. J. **1987**, *22*, 297–340. https://doi.org/10.1002/gj.3350220622.
38. Eugster, H.P.; Wilson, G.A. Transport and deposition of ore-forming elements in hydrothermal systems associated with granites. In High Heat Production Granites, Hydrothermal Circulation and Ore Genesis; Hall, C., Ed.; Inst. Min. Met.: London, UK, 1985; pp. 87–98.
39. Pirajno, F.; Bentley, P.N. Greisen-related scheelite, gold and sulphide mineralisation at Kirwans Hili and Bateman Creek, Reefton district, Westland, New Zealand. *N. Z. J. Geol. Geophys.* **1985**, *28*, 97–109. https://doi.org/10.1080/00288306.1985.10422279.
40. Nambaje, C.; Eggins, S.M.; Yaxley, G.; Sajeev, K. Micro-characterisation of cassiterite by geology, texture and zonation: A case study of the Karagwe Ankole Belt, Rwanda. *Ore Geol. Rev.* **2020**, *124*, 103609. https://doi.org/10.1016/j.oregeorev.2020.103609.
41. Kinnaird, J. A. Hydrothermal Alteration and Mineralisation of the Nigerian Anorogenic Ring Complexes: With Special Reference to the Saiya Shokobo Complex. Ph.D. Thesis, University of St Andrews, St Andrews, Scotland, 1987.
42. Kohút, M.; Recio, C. Sulphur isotope study of selected Hercynian granitic and surrounding rocks from the Western Carpathians (Slovakia). *Geol. Carpathica* **2002**, *53*, 3–13.
43. Salau, L.S. Geology, Geochemistry and Genesis of Gold Mineralization in the Anka Schist Belt, North-Western Nigeria. Ph.D. Thesis, Ahmadu Bello University, Zaria, Nigeria, 2020.
44. Garba, I. Gold prospect of the Nigerian Pan-African terrain of West Africa. *J. Min. Geol*. **2000**, *36*, 123–156.
45. El-Nafaty, J.M. Rare earth element and stable sulphur (δ 34S) isotope study of baryte–Copper mineralization in Gulani area, Upper Benue Trough, NE Nigeria. *J. Afr. Earth Sci*. **2015**, *106*, 147–157. https://doi.org/10.1016/j.jafrearsci.2015.03.007.
46. Crawford, M.L. Phase equilibria in aqueous fluid inclusions. In *Fluid Inclusions: Applications to Petrology*; Hollister, L.S., Crawford, M.L., Eds.; The Mineralogical Association of Canada: Quebec City, QC, Canada, 1981; pp. 75–100.

47. Zarasvandi, A.; Liaghat, S.; Lentz, D.; Hossaini, M. Characteristics of Mineralizing Fluids of the Darreh-Zerreshk and Ali-Abad Porphyry Copper Deposits, Central Iran, Determined by Fluid Inclusion Microthermometry. *Resour. Geol.* **2013**, *63*, 188–209. https://doi.org/10.1111/rge.12004.
48. Hennigh, Q.; Hutchinson, R.W. Cassiterite at Kidd Creek: An example of volcanogenic massive sulfide-hosted tin mineraliza-tion. *Econ. Geol. Monogr.* **1999**, *10*, 431–440. https://doi.org/10.5382/Mono.10.17.
49. Tindle, A.G.; Breaks, F.W. Oxide minerals of the separation rapids rare-element granitic pegmatite group, north-western Ontario. *Can. Mineral.* **1998**, *36*, 609–635.
50. Hoefs, J. *Stable Isotope Geochemistry*, 6th ed.; Springer: Berlin, Germany, 2009; ISBN 978-3-540-70703-5.
51. Roedder, E. *Fluid Inclusions: An Introduction to Studies of All Types of Fluid Inclusions, Gas, Liquid, or Melt, Trapped in Materials from Earth and Space, and Their Application to the Understanding of Geologic Processes*; Reviews in Mineralogy; Mineral Soc. of America: Washington, DC, USA, 1984; ISBN 978-0-939950-16-4.
52. Wilkinson, J. Fluid inclusions in hydrothermal ore deposits. *Lithos* **2001**, *55*, 229–272. https://doi.org/10.1016/s0024-4937(00)00047-5.
53. Dewaele, S.; De Clercq, F.; Muchez, P.; Schneider, J.; Burgess, R.; Boyce, A.; Fernandez Alonso, M. Geology of the cassiterite mineralisation in the Rutongo area, Rwanda (Central Africa): Current state of knowledge. *Geol. Belgica* **2010**, *13*, 91–112.
54. Černý, P.; Blevin, P.L.; Cuney, M.; London, D. Granite-related ore deposits. In *Economic Geology One Hundredth Anniversary Volume*; Hedenquist, J.W., Thompson, J.F.H., Goldfarb, R.J., Richards, J.P., Eds.; Society of Economic Geologists: Littleton, CO, USA, 2005; pp. 337–370. https://doi.org/10.5382/AV100.
55. Hulsbosch, N., Nb-Ta-Sn-W distribution in granite-related ore systems: Fractionation mechanisms and examples from the Karagwe-Ankole belt of Central Africa. In Ore Deposits: Origin, Exploration, and Exploitation, Geophysical Monograph Series, Chapter 4, Decrée S., Robb L. eds.; John Wiley & Sons: New York, USA, 2019; pp. 75–107. https://doi.org/10.1002/9781119290544.ch4.
56. Tillberg, M.; Maskenskaya, O.M.; Drake, H.; Hogmalm, J.K.; Broman, C.; Fallick, A.E.; Åström, M.E. Fractionation of Rare Earth Elements in Greisen and Hydrothermal Veins Related to A-Type Magmatism. *Geofluids* **2019**, *2019*, 1–20. https://doi.org/10.1155/2019/4523214.
57. Rossi, J.N.; Toselli, A.J.; Basei, M.-A.; Sial, A.N.; Baez, M. Geochemical indicators of metalliferous fertility in the Carboniferous San Blas pluton, Sierra de Velasco, Argentina. Geological Society, London, Special Publications **2011**, *350*, 175–186. https://doi.org/10.1144/SP350.10.
58. Ekwere, S.J. Li, F and Rb contents and Ba/Rb and Rb/Sr ratios as indicators of postmagmatic alteration and mineralization in the granitic rocks of the Banke and Ririwai Younger Granite complexes, Northern Nigeria. *Miner. Depos.* **1985**, *20*, 89–93. https://doi.org/10.1007/bf00204315.
59. Girei, M.B.; Li, H.; Algeo, T.J.; Bonin, B.; Ogunleye, P.O.; Bute, S.I.; Ahmed, H.A. Petrogenesis of A-type granites associated with Sn–Nb–Zn mineralization in Ririwai complex, north-Central Nigeria: Constraints from whole-rock Sm Nd and zircon Lu Hf isotope systematics. *Lithos* **2019**, *340–341*, 49–70. https://doi.org/10.1016/j.lithos.2019.05.003.
60. Imeokparia, E.G., Ore-bearing potential of granitic rocks from the Jos-Bukuru Complex, northern Nigeria. Chem. Geol. **1980**, *28*, 69–77. https://doi.org/10.1016/0009-2541(80)90036-4.
61. Neiva, A. Geochemistry of tin-bearing granitic rocks. *Chem. Geol.* **1984**, *43*, 241–256. https://doi.org/10.1016/0009-2541(84)90052-4.
62. Lehmann, B.; Dietrich, A.; Wallianos, A. From rocks to ore. *Geol. Rundsch.* **2000**, *89*, 284–294. https://doi.org/10.1007/s005310000085.
63. Imeokparia, E.G. Fluorine in biotites from the Afu Younger Granite Complex (central Nigeria). *Chem. Geol.* **1981**, *32*, 247–254. https://doi.org/10.1016/0009-2541(81)90147-9.
64. Ishihara, S. The magnetite-series and ilmenite-series granitic rocks. *Min. Geol.* **1977**, *27*, 293–305. https://doi.org/10.11456/shigenchishitsu1951.27.293.
65. Manning, D. The effect of fluorine on liquidus phase relationships in the system Qz-Ab-Or with excess water at 1 kb. *Contrib. Miner. Pet.* **1981**, *76*, 206–215. https://doi.org/10.1007/bf00371960.
66. Watson, E.B.; Harrison, T.M. Zircon saturation revisited: Temperature and composition effects in a variety of crustal magma types. *Earth Planet. Sci. Lett.* **1983**, *64*, 295–304. https://doi.org/10.1016/0012-821X(83)90211-X.
67. Boehnke, P.; Watson, E.B.; Trail, D.; Harrison, T.M.; Schmitt, A.K. Zircon saturation re-revisited. *Chem. Geol.* **2013**, *351*, 324–334. https://doi.org/10.1016/j.chemgeo.2013.05.028.

68. Ishihara, S.; Hashimoto, M.; Machida, M. Magnetite/Ilmenite-series Classification and Magnetic Susceptibility of the Mesozoic-Cenozoic Batholiths in Peru. *Resour. Geol.* **2000**, *50*, 123–129. https://doi.org/10.1111/j.1751-3928.2000.tb00062.x.
69. Ishihara, S. The redox state of granitoids relative to tectonic setting and earth history: The magnetite–ilmenite series 30 years later. *Trans. R. Soc. Edinburgh: Earth Sci.* **2004**, *95*, 23–33. https://doi.org/10.1017/s0263593300000894.
70. Yang, X.-M.; Lentz, D.R.; Chi, G. Ferric-ferrous iron oxide ratios: Effect on crystallization pressure of granites estimated by Qtz-geobarometry. *Lithos* **2020**, *380–381*, 105920. https://doi.org/10.1016/j.lithos.2020.105920.
71. Schmidt, C.; Romer, R.L.; Wohlgemuth-Ueberwasser, C.C.; Appelt, O. Partitioning of Sn and W between granitic melt and aqueous fluid. *Ore Geol. Rev.* **2019**, *117*, 103263. https://doi.org/10.1016/j.oregeorev.2019.103263.
72. Seward, T.M.; Williams-Jones, A.E.; Migdisov, A.A. The Chemistry of Metal Transport and Deposition by Ore-Forming Hydrothermal Fluids. In *Treatise on Geochemistry*, 2nd ed.; Holland, H.D., Turekian, K.K., Eds.; Elsevier: Oxford, UK, 2014; Volume 13, pp. 29–57, ISBN 978-0-08-098300-4.
73. Pirajno, F. Halogens in hydrothermal fluids and their role in the formation and evolution of hydrothermal mineral systems. In *The Role of Halogens in Terrestrial and Extraterrestrial Geochemical Processes*; Harlov, D.E., Aranovich, L., Eds.; Springer Geo-chemistry, Springer: Cham, Germany, 2018; pp. 759–804. https://doi.org/10.1007/978-3-319-61667-4_12.
74. Zajacz, Z.; Halter, W.E.; Pettke, T.; Guillong, M. Determination of fluid/melt partition coefficients by LA-ICPMS analysis of co-existing fluid and silicate melt inclusions: Controls on element partitioning. *Geochim. Cosmochim. Acta* **2008**, *72*, 2169–2197. https://doi.org/10.1016/j.gca.2008.01.034.
75. Wang, R.C.; Yu, A.-P.; Chen, J.; Xie, L.; Lu, J.-J.; Zhu, J.-C. Cassiterite exsolution with ilmenite lamellae in magnetite from the Huashan metaluminous tin granite in southern China. *Miner. Pet.* **2012**, *105*, 71–84. https://doi.org/10.1007/s00710-012-0194-x.
76. Webster, J.; Thomas, R.; Seltmann, R.; Tappen, C. Geochemical evolution of halogen-enriched granite magmas and mineralizing fluids of the Zinnwald tin-tungsten mining district, Erzgebirge, Germany. *Miner. Depos.* **2004**, *39*, 452–472. https://doi.org/10.1007/s00126-004-0423-2.
77. Abaa, S.I. Hydrothermal fluids responsible for the formation of precious minerals in the Nigerian Younger Granite Province. *Miner. Depos.* **1991**, *26*, 34–39. https://doi.org/10.1007/BF00202362.
78. Bachinski, D.J. Bond strength and sulfur isotopic fractionation in coexisting sulfides. *Econ. Geol.* **1969**, *64*, 56–65. https://doi.org/10.2113/gsecongeo.64.1.56.
79. Seal, I.R.R. Sulfur Isotope Geochemistry of Sulfide Minerals. *Rev. Miner. Geochem.* **2006**, *61*, 633–677. https://doi.org/10.2138/rmg.2006.61.12.
80. Driesner, T.; Geiger, S. Numerical Simulation of Multiphase Fluid Flow in Hydrothermal Systems. *Rev. Miner. Geochem.* **2007**, *65*, 187–212. https://doi.org/10.2138/rmg.2007.65.6.
81. Ma, Y.; Xiong, S.-F.; Li, H.-L.; Jiang, S.-Y. Origin and Evolution of the Ore-Forming Fluids in the Liyuan Gold Deposit, Central North China Craton: Constraints from Fluid Inclusions and H-O-C Isotopic Compositions. *Geofluids* **2017**, *2017*, 1–21. https://doi.org/10.1155/2017/3107280.
82. Bodnar, R.J. Introduction to aqueous fluid systems. In *Fluid Inclusions: Analysis and Interpretation*; Sam-son, I., Anderson, A., Marshall, D., Eds.; The Mineralogical Association of Canada: Quebec City, QC, Canada, 2003; 81-ISBN 0-921294-32-8.
83. Borisenko, A.S. Study of the salt composition of solutions in gas-liquid inclusions in minerals by the cryometric method. *Soviet Geol. Geophys.* **1978**, *18*, 11–19.
84. Choi, S.H. Geochemical Evolution of Hydrothermal Fluids at the Daejang Cu-Zn-Pb Vein Deposit, Korea. *Resour. Geol.* **1998**, *48*, 171–182. https://doi.org/10.1111/j.1751-3928.1998.tb00015.x.
85. Urubek, T.; Dolníček, Z.; Kropáč, K. Genesis of Syntectonic Hydrothermal Veins in the Igneous Rock of Teschenite Association (Outer Western Carpathians, Czech Republic): Growth Mechanism and Origin of Fluids. *Geol. Carpathica* **2015**, *65*, 419–431. https://doi.org/10.1515/geoca-2015-0003.
86. Chen, L.-L.; Ni, P.; Dai, B.-Z.; Li, W.-S.; Chi, Z.; Pan, J.-Y. The Genetic Association between Quartz Vein- and Greisen-Type Mineralization at the Maoping W–Sn Deposit, Southern Jiangxi, China: Insights from Zircon and Cassiterite U–Pb Ages and Cassiterite Trace Element Composition. *Minerals* **2019**, *9*, 411. https://doi.org/10.3390/min9070411.
87. Murciego, A.; Sanchez, A.G.; Dusausoy, Y.; Pozas, J.M.M.; Ruck, R. Geochemistry and EPR of cassiterites from the Iberian Hercynian Massif. *Miner. Mag.* **1997**, *61*, 357–365. https://doi.org/10.1180/minmag.1997.061.406.03.
88. Zoheir, B.A. Microchemistry and stable isotope systematics of gold mineralization in a gabbro–diorite complex, SE Egypt. *Microchem. J.* **2012**, *103*, 148–157. https://doi.org/10.1016/j.microc.2012.02.003.

89. Yang, F.; Zhai, W.; Sun, X.; Klemd, R.; Sun, Y.; Wu, Y.; Hua, R.; Zheng, S. Fluid Inclusions and Stable Isotopic Characteristics of the Yaoling Tungsten Deposit in South China: Metallogenetic Constraints. *Resour. Geol.* **2018**, *69*, 107–122. https://doi.org/10.1111/rge.12188.
90. Xu, T.; Wang, Y. Sulfur and lead isotope composition on tracing ore-forming materials of the Xihuashan tungsten deposit in Southern Jiangxi. *Bull. Miner. Pet. Geochem.* **2014**, *33*, 342–347. https://doi.org/10.3969/j.issn.1007-2802.2014.03.008. (In Chinese with English abstract)
91. Cai, Y.; Ma, D.S.; Lu, J.J.; Huang, H.; Zhang, R.Q.; Qu, W.J. Re-Os geochronology and S isotope geochem-istry of Dengfuxian tungsten deposit, Hunan Province, China. *Acta Pet. Sin.* **2012**, *28*, 3798–3808. (In Chinese with English abstract)
92. Reed, M.H. Sulfide Mineral Precipitation from Hydrothermal Fluids. *Rev. Miner. Geochem.* **2006**, *61*, 609–631. https://doi.org/10.2138/rmg.2006.61.11.
93. Plümper, O.; Putnis, A. The Complex Hydrothermal History of Granitic Rocks: Multiple Feldspar Replacement Reactions under Subsolidus Conditions. *J. Pet.* **2009**, *50*, 967–987. https://doi.org/10.1093/petrology/egp028.
94. Stevenson, C. The relationship between forceful and passive emplacement: The interplay between tectonic strain and magma supply in the Rosses Granitic Complex, NW Ireland. *J. Struct. Geol.* **2009**, *31*, 270–287. https://doi.org/10.1016/j.jsg.2008.11.009.
95. Chicharro, E.; Boiron, M.-C.; López-García, J.; Barfod, D.N.; Villaseca, C. Origin, ore forming fluid evolution and timing of the Logrosán Sn–(W) ore deposits (Central Iberian Zone, Spain). *Ore Geol. Rev.* **2016**, *72*, 896–913. https://doi.org/10.1016/j.oregeorev.2015.09.020.
96. Du, Y.; Qin, X.; Barnes, C.G.; Cao, Y.; Dong, Q.; Du, Y. Sulphide melt evolution in upper mantle to upper crust magmas, Tongling, China. *Geosci. Front.* **2014**, *5*, 237–248. https://doi.org/10.1016/j.gsf.2013.06.003.
97. Giaccherini, A.; Montegrossi, G.; Di Benedetto, F. Stability of Naturally Relevant Ternary Phases in the Cu–Sn–S System in Contact with an Aqueous Solution. *Minerals* **2016**, *6*, 79. https://doi.org/10.3390/min6030079.
98. Kinnaird, J.A.; Nex, P.A.; Milani, L. Tin in Africa. *Episodes* **2016**, *39*, 361–380. https://doi.org/10.18814/epiiugs/2016/v39i2/95783.
99. Amuda, A.K.; Yang, X.; Deng, J.; Faisal, M.; Cao, J.; Bute, S.I.; Girei, M.B.; Elatikpo, S.M. Petrogenesis of the peralkaline Dutsen Wai and Ropp complexes in the Nigerian younger granites: Implications for crucial metal enrichments. *Int. Geol. Rev.* **2020**, *63*, 2057–2081. https://doi.org/10.1080/00206814.2020.1821250.